RSC Advances

REVIEW

View Article Online
View Journal | View Issue

Open Access Article. Published on 16 October 2023. Downloaded on 8/7/2025 12:39:15 AM.
This article is licensed under a Creative Commons Attribution-NonCommercial 3.0 Unported Licence.

Check for updates

Cite this: *RSC Adv.*, 2023, **13**, 30133

X-ray excited luminescent nanoparticles for deep photodynamic therapy

Bang Yao,[ab] Xiaoxu Liu,*[a] Wenli Zhang*[b] and Hongbing Lu*[b]

Photodynamic therapy (PDT), as a non-invasive treatment, has received wide attention because of its high selectivity and low side effects. However, traditional PDT is influenced by the excitation light source and the light penetration depth is limited, which can only be used for superficial epidermal tumor treatment, and it is still a great challenge for deep tumor treatment. In recent years, X-ray excitation photodynamic therapy (X-PDT) using penetrating X-rays as an external excitation source and X-ray excited luminescent nanoparticles (XLNP) as an energy transfer medium to indirectly excite photosensitizer (PS) has solved the problem of insufficient penetration depth in tissues and become a research hotspot in the field of deep tumor treatment. In this review, the recent research progress of nanoparticles for efficient X-PDT, listing different types of XLNP and luminescence enhancement strategies. The loading method of PS is highlighted to achieve efficient energy transfer by regulating the intermolecular distance between both XLNP/PS. In addition, the water-soluble modification of XLNP surface is discussed and different hydrophilic modification methods are proposed to provide reference ideas for improving the dispersibility and biocompatibility of XLNP in aqueous solution. Finally, the therapeutic effects about X-PDT are discussed, and the current challenges and future perspectives for its clinical applications are presented.

Received 24th July 2023
Accepted 22nd September 2023

DOI: 10.1039/d3ra04984a

rsc.li/rsc-advances

1. Introduction

Cancer is one of the deadliest diseases in the world. The traditional clinical treatment is based on surgical resection, supplemented by adjuvant treatments such as chemotherapy and radiotherapy. However, chemotherapeutic drugs have toxic side effects and high doses of X-ray radiation may cause damage to normal tissues.[1] Therefore, researchers are actively exploring new therapeutic approaches to solve the current problems. Photodynamic therapy (PDT) has the advantages of being less invasive, shorter treatment time, and higher tissue selectivity. Moreover, it has been approved for clinical use in the treatment of a wide range of cancers due to its high safety and low toxicity to normal tissues compared to chemotherapy and radiotherapy.[2] Among them, there are three key factors affecting the efficacy of PDT, which are excitation light, oxygen content, and photosensitizer (PS). PS produces cytotoxic reactive oxygen species (ROS), especially singlet oxygen ($^1O_2$) under light irradiation in the appropriate wavelength range leading to apoptosis or necrosis of tumor cells for therapeutic purposes.[3,4] However, the absorption wavelength range of PS used for conventional PDT is located in the ultraviolet (10–390 nm) or visible light (390–770 nm) region, and because the penetration depth of light in this wavelength range is very limited in biological tissues (<5 mm), this limits photodynamic therapy to the treatment of tumors in superficial tissue areas and makes it difficult to perform non-invasive treatment of deep or excessively thick or large tumors.[5] Notably, the near-infrared (NIR) biological window is a tissue-transparent window located at about 780–1100 nm, which can effectively avoid absorption and scattering by biological tissues and has a strong penetrating ability. However, for practical applications, due to the strong thermal effect of NIR, NIR light can still only effectively penetrate 15 mm of tissue while considering thermal effects and residual excitation energy.[6]

X-rays, as a highly penetrating electromagnetic wave, have the advantage of unrestricted penetration depth in tissues compared to ultraviolet, visible and near-infrared light. For this reason, researchers have introduced X-rays as an excitation source for photodynamic therapy, called X-ray excited photodynamic therapy (X-PDT).[7] Therefore, researchers introduced X-rays as an excitation light source for photodynamic therapy, called X-ray excited photodynamic therapy (X-PDT).[7] However, since most of the PS cannot absorb the energy of X-rays directly, only some high atomic number X-ray excited luminescent nanoparticles (XLNP) can be used as energy converters to convert the high-energy photons of X-rays into low-energy photons such as UV/visible light to excite the photosensitizers to produce ROS. The luminescence process of XLNP can be summarized into three stages: (1) the conversion of high-energy ionizing radiation to electron–hole pairs; (2) the transfer of energy from the matrix to the luminescent central ion; and (3) the luminescence process of the activated luminescent

[a]School of Materials Science and Engineering, Shaanxi University of Science and Technology, Xian 710021, China. E-mail: xiaoxuliu@sust.edu.cn

[b]School of Biomedical Engineering, Shaanxi Provincial Key Laboratory of Bioelectromagnetic Detection and Intelligent Perception, The Fourth Military Medical University, 169th Changle West Road, Xi'an, Shaanxi 710032, China. E-mail: wenli1121@fmmu.edu.cn; luhb@fmmu.edu.cn

© 2023 The Author(s). Published by the Royal Society of Chemistry

Open Access Article. Published on 16 October 2023. Downloaded on 8/7/2025 12:39:15 AM.
This article is licensed under a Creative Commons Attribution-NonCommercial 3.0 Unported Licence.

central ion.[8] This part will be described in detail in a later paper. A variety of XLNP have been developed, such as rare earth element-based nanoparticles (LaF_3, $NaYF_4$, $Gd_2(WO_4)_3$, *etc.*), metal–oxygen (sulfide) semiconductor nanoparticles (ZnO, $ZnGa_2O_4$:Cr^{3+}, *etc.*), quantum dots (CdTe, CdSe, *etc.*), chalcogenides ($CsPbBr_3$, Rb_2CuBr_3), metal–organic frameworks (MOF), and organic scintillators, *etc.*

In order to achieve efficient X-PDT treatment, an appropriate amount of PS should be piggybacked onto the surface of XLNP, and effective energy transfer from XLNP to PS should be achieved through a fluorescence resonance energy transfer (FRET) process. However, the XLNP used should meet several conditions: (a) the emission spectra of XLNP must match the absorption spectra of PS, which are stably coupled to XLNP by optimizing the loading strategy of PS to ensure effective activation of PS and more $^1O_2$ production. (b) XLNP must have high luminescence efficiency under X-ray excitation so that sufficient energy is available for PS activation. (c) Water-soluble modification of the XLNP surface to increase their dispersibility in water and ensure good biocompatibility. (d) XLNP and PS need to ensure low toxicity.[9] There are also materials based on metal complexes and organic scintillators that can be directly activated by X-rays, now called Radiodynamic Therapy (abbreviated as RDT). They mainly perform energy transfer in nanomaterials to produce $^1O_2$, $\cdot O_2$, and $\cdot OH$. Taking directly activatable photosensitizers as an example, such as Cu-Cy, achieving therapeutic effects usually requires a high dose of X-ray irradiation, mainly due to the inefficient energy conversion that does not allow an effective production of ROS. Since the ultimate goal of X-PDT is clinical application, the targeted delivery of XLNP-PS coupling system to tumor sites is crucial. Current research has focused on the use of nanoparticles (NPs) as PS carriers to enhance passive targeting. For passive targeting, NPs tend to have a long cycle time and are more enriched in the tumor environment only through enhanced permeability and retention effect (EPR).[10,11] Therefore, increasing their active targeting function can be considered by modifying the surface of NPs with various targeting ligands, such as adding antibodies or antibody fragments that recognize specific surface receptors on tumor cells to enhance targeting uptake efficiency.

This paper reviews the recent advances in X-ray excited luminescent nanoparticles for deep tumor therapy in PDT. The types of X-ray excited luminescent nanoparticles, luminescence principles, photosensitizer loading strategies, surface water-soluble modification methods and photodynamic therapy effects that have been reported in recent years are highlighted, while the main issues and challenges regarding the current deep tumor photodynamic therapy are discussed, and the future directions of development are foreseen (Fig. 1).

2. Luminescent nanoparticles in X-PDT

2.1 Principle of the role of XLNP and PS in PDT

The premise of efficient X-PDT is that XLNP can absorb a large amount of X-ray energy and emit light that matches the absorption spectrum of the photosensitizer.[12,13] The action process of X-PDT is shown in Fig. 2: firstly, XLNP and photosensitizers with mutually matching emission and absorption spectra are selected, and PS is loaded onto the surface of XLNP by covalent bonding or physical adsorption to obtain XLNP/PS nanocomplex. Then, they are injected into the body and actively targeted by targeting molecules to guide the luminescent nanoparticle-photosensitizer coupling system to enrich at the tumor site, and passively targeted by the EPR effect to enrich at the tumor site.

When XLNP are radiated with X-rays, the most part of incident X-ray energy will be absorbed by XLNP and tissues, a little part will be absorbed by photosensitizer, in the contrast, some of the incident X-ray will penetrate the target tissue as well, the portion of X-ray energy absorbed is highly related with the incident X-ray energy. The XLNP will generate UV-Vis light upon X-ray excitation, the energy is transferred to the photosensitizer through the FRET process to produce photodynamic effect, which can be divided into type I and type II reactions according to the nature of the photosensitizer itself, and generates a large amount of reactive oxygen species (ROS) that can efficiently oxidize biomolecules (such as unsaturated fatty acids, proteins, cell membranes and mitochondrial membranes, *etc.*), thus inducing tumor cell apoptosis/necrosis.

In X-PDT, XLNP produce UV-visible light and two types of reactions occur when the PS absorbs energy. The electron transitions from the ground state (S_0) to the excited singlet state (S_1).[14] The excited state of the photosensitizer can decay back to the ground state by emitting fluorescence, a feature that can be applied to bioimaging and photodetection. A part, on the other hand, transfers the excited electrons to the triplet excited state (T_1) with a relatively long half-life by inter-system scramble (ISC). This excited triplet state electron triggers the photochemical reaction through two different (type I and type II) pathways, as shown in Fig. 3. In the type I reaction, the PS excited triplet state is involved in the electron transfer process, interacting directly with the substrate (*e.g.*, cell membrane or molecules) to form radicals, and then interacting with triplet oxygen ($^3O_2$) and water to produce superoxide anion ($-O_2$), hydroxyl radical (–OH), and hydrogen peroxide (H_2O_2), *etc*. In addition, in the type II reaction, the PS excited triplet state can also undergo energy transfer directly with oxygen ($^3O_2$) to generate cytotoxic singlet oxygen ($^1O_2$), which contributes to apoptosis of tumor cells. Notably, type I and type II reactions can occur simultaneously, and the ratio of the two reactions depends on the nature of PS, the substrate and oxygen concentration.[15] Also, type II reactions predominate in well oxygenated environments, while type I reactions can occur under hypoxic conditions.

2.2 Physical process of luminescence of XLNP

The luminescence mechanism of XLNP can be summarized into three stages: conversion, transmission and luminescence. Taking lanthanide luminescent nanoparticles as an example, as shown in Fig. 4, firstly, in the conversion phase, high-energy X-ray photons interact with the lattice of XLNP through photoelectric and Compton scattering effects, and generate a large

 © 2023 The Author(s). Published by the Royal Society of Chemistry

Open Access Article. Published on 16 October 2023. Downloaded on 8/7/2025 12:39:15 AM.
This article is licensed under a Creative Commons Attribution-NonCommercial 3.0 Unported Licence.

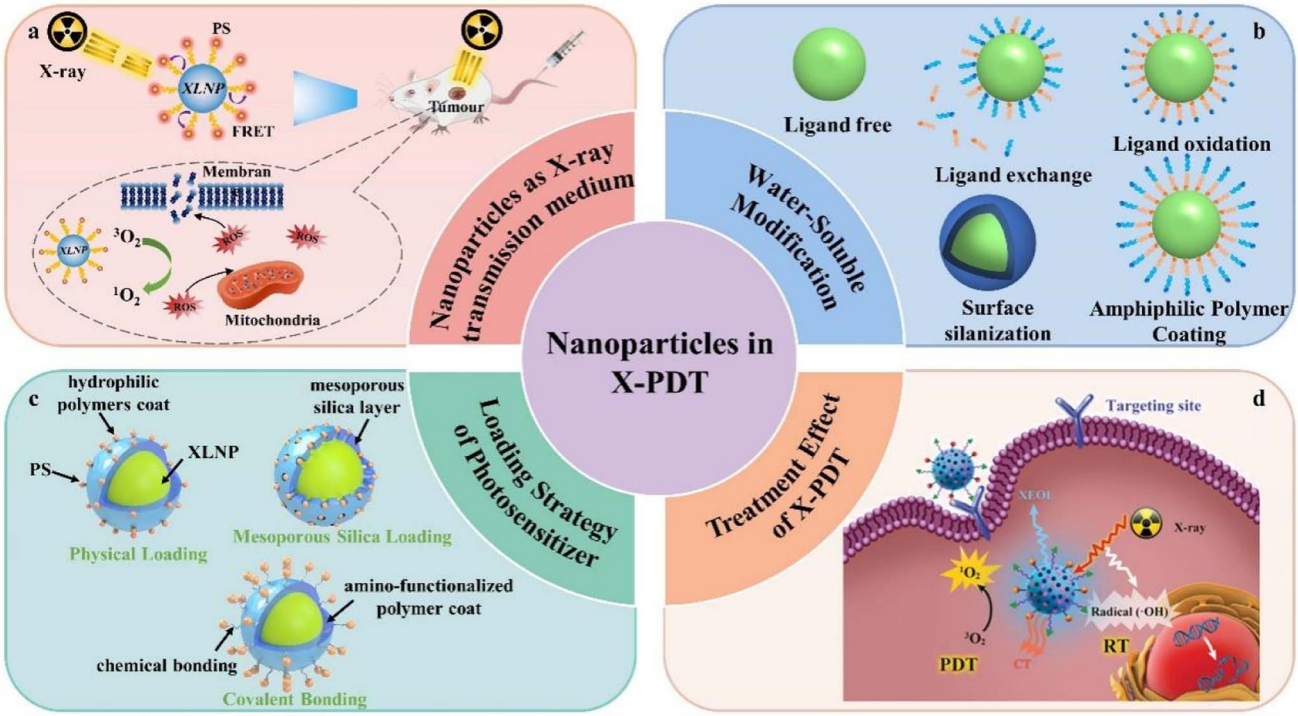

Fig. 1 Application of nanoparticles in X-PDT: (a) nanoparticles as X-ray transmission medium, (b) water-soluble modification, (c) loading strategy of photosensitizer, (d) treatment effect of X-PDT.[68]

number of secondary electrons through electron pair effects and Osher reactions, leading to the gradual thermalization of hot electrons and holes generated in the process at the conduction and valence band edges, respectively, and the production of many electron–hole pairs.[16–18] During the transport phase, the luminescence centers perform successive trapping of electrons and holes, such as the formation of ionic vacancies, surface defects, or Frenkel defects. These defects may

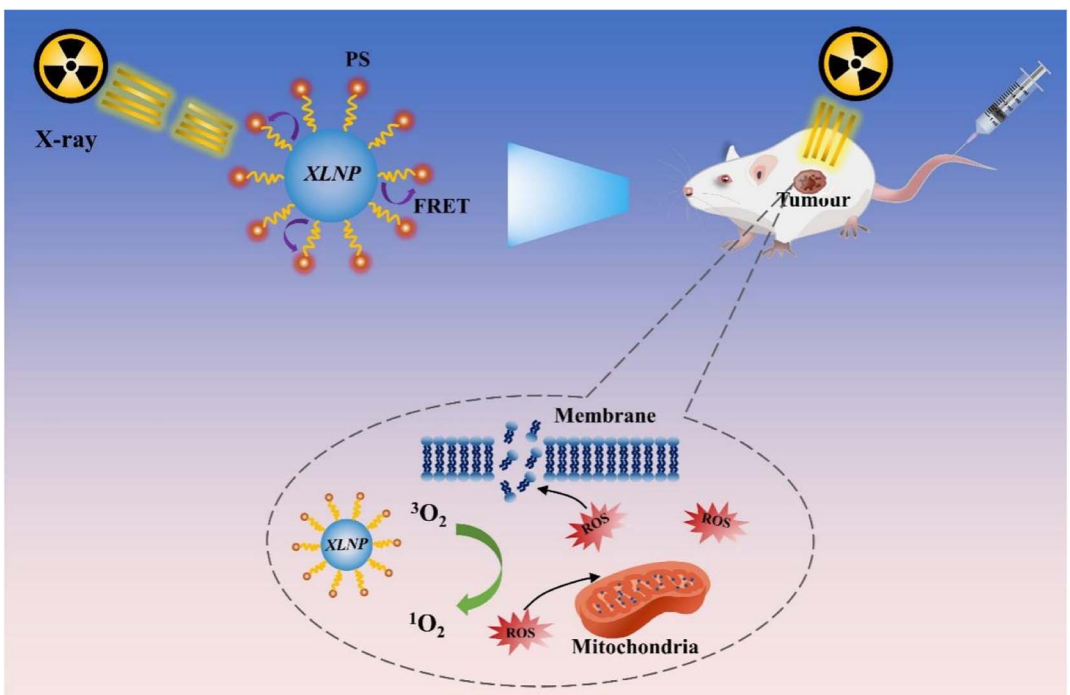

Fig. 2 Schematic diagram of luminescent nanoparticles as X-ray transmission medium applied to X-PDT.

Open Access Article. Published on 16 October 2023. Downloaded on 8/7/2025 12:39:15 AM.
This article is licensed under a Creative Commons Attribution-NonCommercial 3.0 Unported Licence.

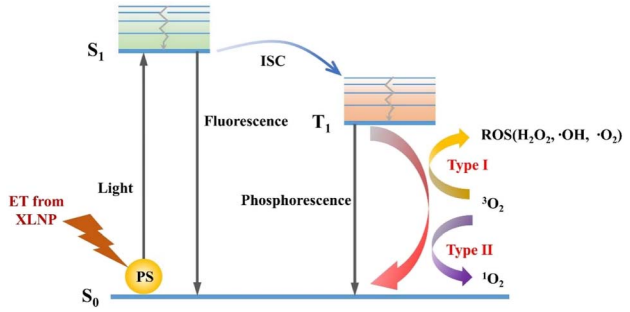

Fig. 3 Mechanism of XLNP indirect excitation of X-PDT.

lead to energy loss in the form of non-radiative relaxation as well as other mechanisms that reduce the luminescence intensity, but also contribute to the afterglow. It is generally believed that afterglow facilitates improved signal-to-noise ratio, reduces tissue spontaneous-induced fluorescence background interference, and produces high-contrast imaging, which shows promising applications in biomedicine. Due to thermal perturbation, the electron–hole pairs captured at the defects are slowly released, and the electrons and holes are transferred to the conduction band and valence band, respectively, and then migrate toward the lanthanide element activator. In the final luminescence stage, the excitation energy level of the lanthanide activator achieves luminescence by absorbing the energy released from the recombination of the trapped electron–hole pairs through 5d–4f or 4f–4f transitions.

Combined with the luminescence principle of XLNP in Fig. 4, the luminescence intensity of the material is directly related to the X-ray absorption efficiency. The X-ray absorption coefficient (α) is the efficiency of the nanoscintillation particle in absorbing the energy of incident X-ray photons during the conversion phase and can be expressed by eqn (1):[19]

$$\alpha = \rho Z^4 / A E^3 \quad (1)$$

where ρ denotes density, Z is atomic number, A is atomic mass, and E is X-ray photon energy. From the equation, it can be seen that the selection of nanoscintillation particles with high density (ρ) and high atomic number (Z) is favorable to improve the absorption efficiency of X-rays and enhance their emission intensity.

2.3 Types of luminescent nanoparticles

2.3.1 Rare earth element-based nanoparticles. Rare earth ions have abundant ladder energy levels and can produce luminescence in different wavelength bands from UV and visible to near-infrared light by 4f–4f or 4f–5d transitions.[20] Among them, X-ray excited lanthanide nanoscintillation particles with narrow spectral lines, pure chromaticity and long fluorescence lifetime are used in bioimaging and X-PDT therapy. At present, various nanoscintillation particles have been successfully synthesized by doping lanthanides into different host matrices, mainly including rare earth metal fluorides (LaF_3, CeF_3, GdF_3, *etc.*), alkali metal fluorides of rare earth metals ($NaYF_4$, $NaLuF_4$, *etc.*), rare earth metal oxides (Y_2O_3, Tb_2O_3, *etc.*), rare earth metal sulfide oxides (Gd_2O_2S) and rare earth metal tungstate ($Gd_2(WO_4)_3$), *etc.*

The nature of the nanoparticle host matrix and its interaction with the dopant ions have a great influence on the luminescence efficiency. The direct choice of the host matrix determines the distance between the dopant ions, their relative spatial position and coordination number.[21–23] The ideal host matrix material should have a low lattice phonon energy that minimizes nonradiative relaxation and maximizes radiative emission. For example, some heavy halides such as chlorides, bromides, and iodides usually exhibit low phonon energies below 300 cm^{-1}. However, they are hygroscopic and have limited use. Oxides have high chemical stability, but they have relatively high phonon energies, typically greater than 500 cm^{-1}, due to the stretching vibrations of the host lattice. In comparison, fluoride materials have low lattice phonon energies (~350 cm^{-1}) and exhibit high luminescence efficiency and long lifetime of the excited state when doped with lanthanide ions.[24] For rare earth metal fluorides, they can be prepared by well-established and simple chemical synthesis methods such as co-precipitation, solvent/hydrothermal and thermal

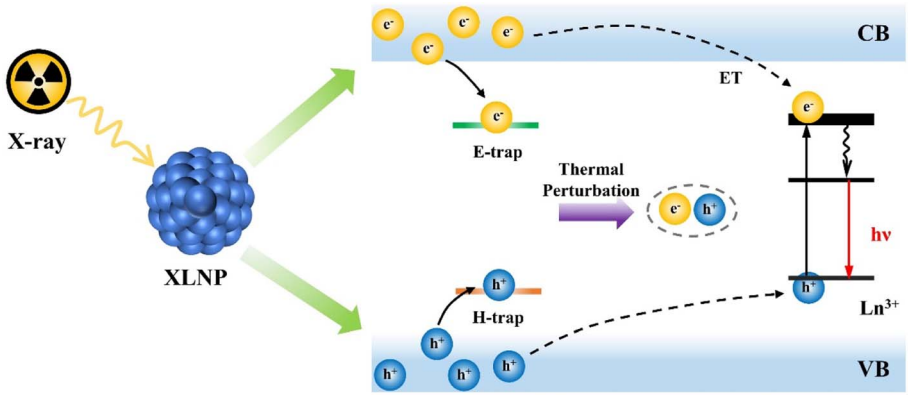

Fig. 4 Schematic diagram of the luminescence process of XLNP. CB, conduction band; VB, valence band. ET, energy transfer between lanthanide ions.

 © 2023 The Author(s). Published by the Royal Society of Chemistry

Open Access Article. Published on 16 October 2023. Downloaded on 8/7/2025 12:39:15 AM.
This article is licensed under a Creative Commons Attribution-NonCommercial 3.0 Unported Licence.

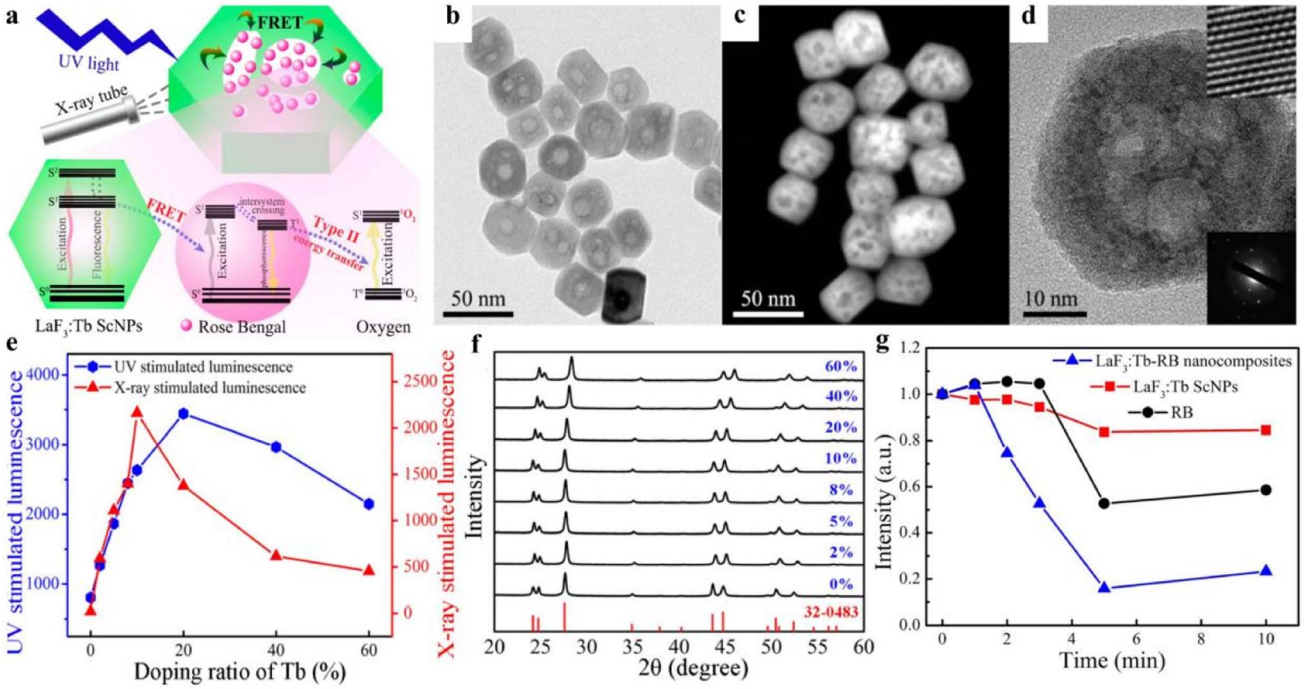

Fig. 5 (a) Schematic diagram of the structure of mesoporous LaF_3:Tb-RB nanocomposites and their application in PDT; (b) TEM images of mesoporous LaF_3:Tb nanoparticles, (c) SEM images; (d) HR-TEM images and SAED images; (e) UV and X-ray excitation of LaF_3:Tb nanoparticles with different concentrations of Tb^{3+} doped luminescence intensity; (f) characterizations of mesoporous LaF_3:Tb ScNPs with varied Tb^{3+} doping ratio corresponding XRD patterns; (g) decrease of emission intensity of DPBF treated with LaF_3:Tb ScNPs, RB, and LaF_3:Tb-RB nanocomposites, respectively, after different irradiation time.[26]

decomposition methods, which enable controlled adjustment of their particle size, shape, crystalline phase and chemical composition. Moreover, this type of nanoparticles has excellent photostability and low toxicity. These properties make it promising for medical imaging and X-PDT therapy. In 2006, Chen *et al.*[7] first proposed X-ray excited scintillation nanoparticles loaded with photosensitizers to be used as *in vivo* reagents for photodynamic therapy. They attached particles such as LaF_3:Ce^{3+} and LuF_3:Ce^{3+} to porphyrin-based photosensitizers by covalent bonding and delivered the photosensitizers to the treatment site using a folic acid modified targeting group. The X-ray irradiated nanoscintillators emit ultraviolet light and activate the coupled photosensitizers, producing $^1O_2$ to kill cancer cells. This study is an innovative proposal to attach scintillation nanoparticles to a photosensitizer, enabling photodynamic therapy without the use of an external light source. In 2008, Chen's group reported on the synthesis of X-ray excited LaF_3:Ce^{3+},Tb^{3+} NPs.[25] During the synthesis, water-soluble LaF_3:Tb^{3+}/AA_{11} NPs with diameters of 15–20 nm were prepared by adding H_2N–$(CH_2)_{10}$–COOH (AA_{11}) chains as stabilizers. Luminescence intensity compared to LaF_3:Tb. This may be due to the fact that the coating of AA_{11} layer on the nanoparticle surface can reduce the X-ray excited fluorescence quenched and enhance the luminescence intensity of the nanoparticles.

The high efficiency of energy transfer between the luminescent nanoparticles and the photosensitizer is more effective in activating the photosensitizer, producing more $^1O_2$ and improving the efficiency of X-PDT. For example, Tang *et al.*[26] synthesized mesoporous LaF_3:Tb^{3+} NPs by hydrothermal method. As seen from the TEM and SEM images in Fig. 5b–d, the synthesized nanoparticles are uniform in size, regular hexagonal or spherical in shape, and exhibit an obvious porous structure with an average particle size of about 38.9 nm. Although LaF_3:Tb^{3+} NPs were synthesized The LaF_3:Tb^{3+} NPs were prepared by a simple hydrothermal method without the use of catalysts, surfactants or templating agents in the synthesis process. However, the nanoparticles are highly stable in water due to the presence of a large amount of unsaturated Ln^{3+} on their surface, which makes them positively charged. The obtained nanoparticles also exhibited good water dispersion and stability. The optimized LaF_3:Tb^{3+} NPs can emit intense green light under both UV and X-ray excitation. As shown in Fig. 5e, the X-ray excitation fluorescence intensity of LaF_3:Tb^{3+} NPs reached the maximum when the doping concentration of Tb^{3+} reached 10%. In Fig. 5f, the XRD analysis results of the samples with different percentages of Tb^{3+} doping are consistent with the pure hexagon of LaF_3. RB was attached to LaF_3:Tb^{3+} NPs by a porous loading method to enhance the fluorescence resonance energy transfer (FRET) efficiency (up to more than 85%). Under X-ray irradiation, a large amount of $^1O_2$ was generated, and the LaF_3:Tb-RB nanocomposites showed increased $^1O_2$ production compared to RB alone (Fig. 5g). It demonstrated the great potential of this system for PDT treatment of deep tumors.

Open Access Article. Published on 16 October 2023. Downloaded on 8/7/2025 12:39:15 AM.
This article is licensed under a Creative Commons Attribution-NonCommercial 3.0 Unported Licence.

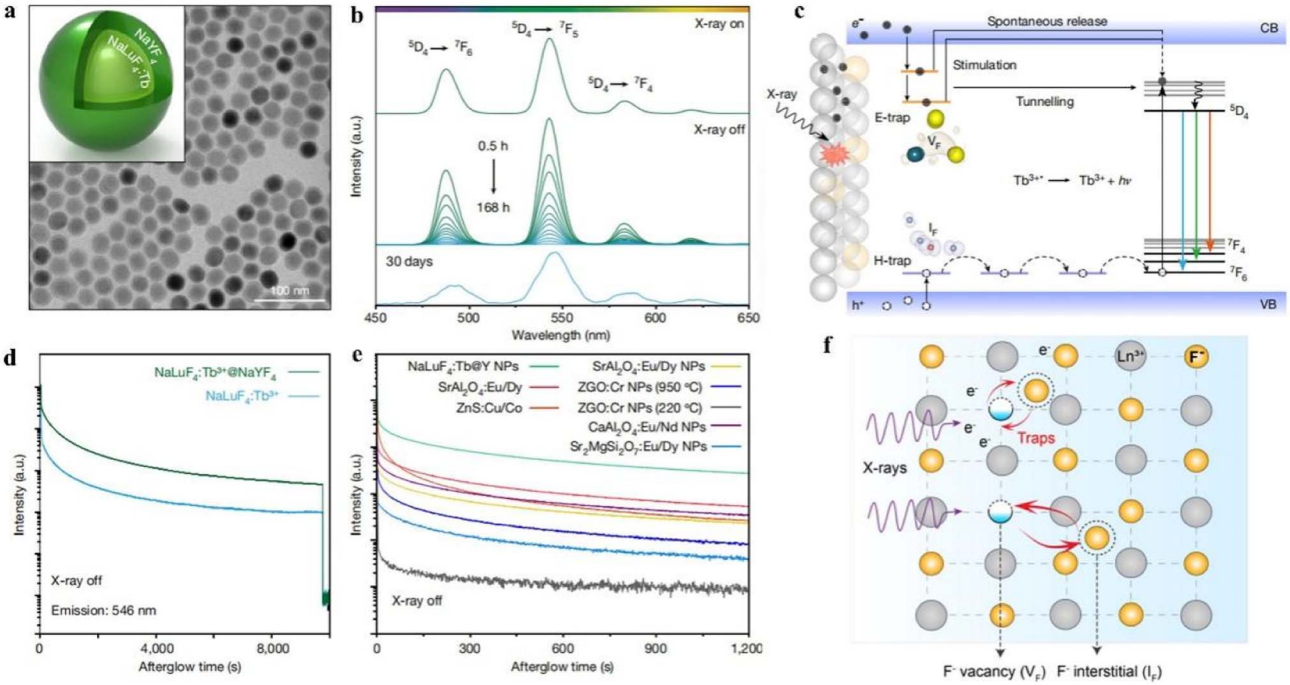

Fig. 6 (a) TEM images of $NaLuF_4$:Tb@$NaYF_4$ NPs; (b) radioluminescence emission spectra of $NaLuF_4$:Tb@$NaYF_4$ NPs after 50 kV stop X-ray irradiation for 0.5–168 h or 30 days; (c) mechanism of sustained luminescence of Tb^{3+}-doped $NaLuF_4$ NPs; (d) variation of radioluminescence intensity with time for $NaLuF_4$:Tb and $NaLuF_4$:Tb@$NaYF_4$ nanocrystals at 546 nm as a function of time; (e) afterglow decay curves of different phosphors after 50 kV X-ray excitation; (f) generation of Frenkel trap states in $NaLuF_4$ lattice under X-ray irradiation. The small fluoride ions (F^-) then migrate from the lattice to the interstitial sites. This leads to the production of many fluoride vacancies (V_F) and interstitials (I_F) and is accompanied by the capture of high-energy electrons (e^-) at the defects.[28]

The luminescence efficiency can also be enhanced by building multilayer core–shell structures in synthetic luminescent nanomaterials to extend the energy diffusion distance and reduce fluorescence quenched, and it can also extend the luminescence lifetime to achieve sustained luminescence.[27] Sustained luminescence can continue to emit light for minutes or even hours after the excitation light source is turned off, is not disturbed by background fluorescence, has a low signal-to-noise ratio, and the material can generate ROS long after excitation, making it suitable for use in high-contrast bioimaging and X-PDT. For example, Ou *et al.*[28] synthesized $NaLuF_4$:Tb@$NaYF_4$ NPs using a co-precipitation method, and TEM images showed that their average particle size was 27 nm with regular morphology and uniform distribution (Fig. 6a). Under the excitation of a 50 kV X-ray source (Fig. 6b), their radioluminescence was measured and showed three typical emission peaks attributed to the $^5D_4 \rightarrow {}^7F_4$ (584 nm), $^5D_4 \rightarrow {}^7F_5$ (546 nm) and $^5D_4 \rightarrow {}^7F_6$ (489 nm) transitions. In addition, the afterglow properties of $NaLuF_4$:Tb@$NaYF_4$ NPs were tested, and the luminescence persisted for more than 30 days after the X-ray excitation stopped (Fig. 6b, bottom). And in comparison with commercial scintillators and conventional long afterglow phosphors, $NaLuF_4$:Tb@$NaYF_4$ NPs showed stronger X-ray induced emission and afterglow luminescence (Fig. 6e). The mechanism of their sustained luminescence is proposed in Fig. 6c and f. In $NaLuF_4$:Tb@$NaYF_4$ NPs, Lu atoms produce many high-energy electrons after absorbing X-ray energy, which form electron traps (E traps) and hole traps (H traps) in the nanocrystals by elastic collisions of large momentum X-ray photons with small fluorine ions and trap thermalized low-energy electrons and holes. When the excitation source is turned off, the electrons and holes in the traps escape to the conduction and valence bands, and electron–hole pair compounding occurs to release energy, which results in continuous luminescence of XLNP. Among them, the energy and number of traps will directly determine the intensity and duration of the remaining glow. Secondly, the effective isolation of the activator from the surface quencher by encapsulating the $NaYF_4$ inert shell can alleviate the quenched of X-ray energy trapped on the surface of the nanocrystal. $NaLuF_4$:Tb@$NaYF_4$ NPs are composed of a core formed by a lanthanide-doped matrix and some non-rare earth-doped inert shells. Such heavy metal-containing core–shell nanomaterials have strong X-ray blocking and absorbing effects, and thus can be used as X-ray excited luminescent materials in PDT. However, more *in vitro*/*in vivo* experiments are needed to confirm the practicality of X-ray excited PDT therapy.

Furthermore, Xie *et al.*[29] reported a $SrAl_2O_4$:Eu^{2+} (SAO) nanoparticle-mediated X-ray induced photodynamic *in vivo* treatment of cancer. As shown in Fig. 7a and b, $SrAl_2O_4$:Eu^{2+} (SAO) was firstly obtained from nanowires by carbon reduction reaction by vapor phase deposition, and particles with a particle size of about 80 nm were obtained by grinding, settling and centrifugation. Then a layer of dense silica and mesoporous silica were coated on

 © 2023 The Author(s). Published by the Royal Society of Chemistry

Open Access Article. Published on 16 October 2023. Downloaded on 8/7/2025 12:39:15 AM.
This article is licensed under a Creative Commons Attribution-NonCommercial 3.0 Unported Licence.

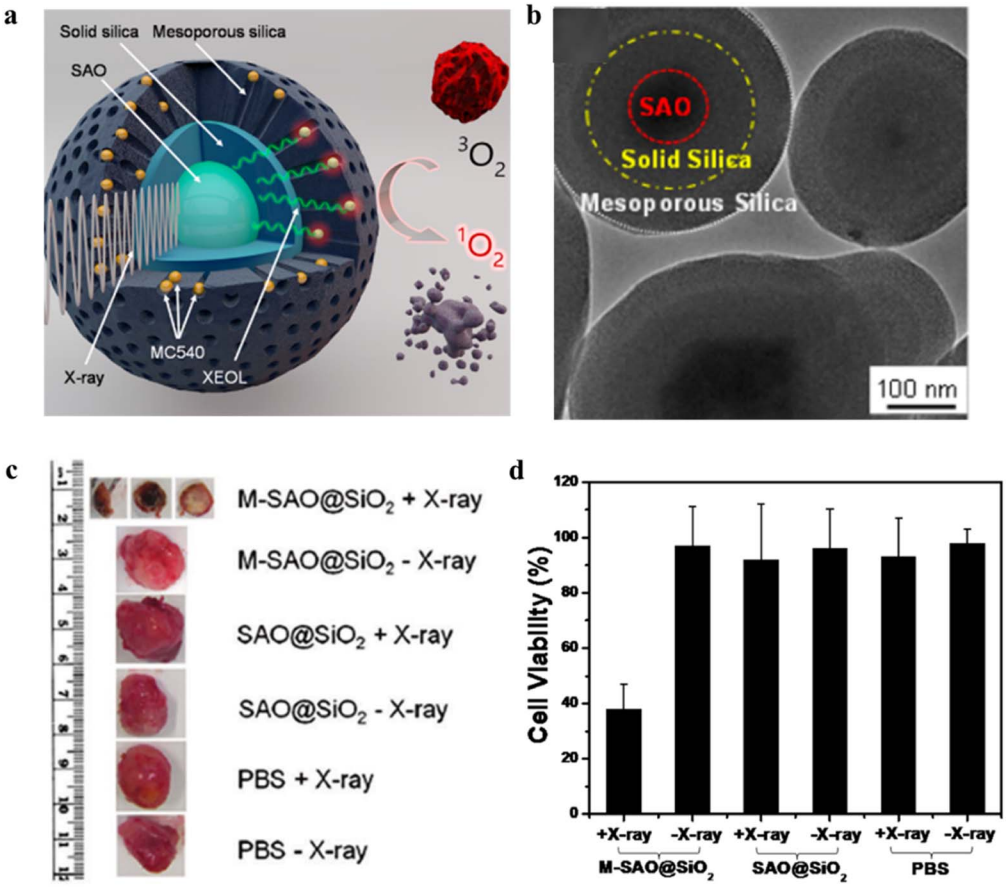

Fig. 7 (a) Schematic diagram of X-PDT of SAO@SiO_2-MC540 nanocomposites; (b) TEM images of SAO@SiO_2 nanoparticles; (c) representative tumors after X-PDT photograph; (d) cell viability of U87MG after different treatments.[29]

its surface, respectively, and then Merocyanine 540 (MC540) was loaded into the mesopores (noted as M-SAO@SiO_2), and the obtained SAO with a particle size of about 407.4 ± 152.5 nm. In *in vitro* and *in vivo* assays, it was found that low dose X-ray (0.5 Gy) irradiation could significantly decrease cell viability by 62.0 ± 9.0%. And significant tumor growth arrest and even atrophy were observed in a mouse U87MG xenograft model, while normal tissues were unaffected (Fig. 7c and d). Since SAO nanoparticles are highly hydrolytic, the treated SAO nanoparticles were decomposed into low-toxic ions for removal from the host body without other side effects arising.

2.3.2 Metal-sulfur/oxide semiconductor nanoparticles. In addition to rare earth element-based nanoscintillation particles, some metal-sulfur/oxide semiconductor nanoparticles can also be excited by X-rays to produce specific wavelengths of light to activate photosensitizers to produce reactive oxygen species (ROS) for photodynamic therapy. For example, ZnO nanoparticles can be excited by X-rays to emit intense fluorescence and their emission wavelength range matches the absorption spectrum of porphyrin-based photosensitizers for X-PDT therapy. Chen *et al.*[25] prepared ZnO nanoparticles, which were conjugated with porphyrin-derived photosensitizers (MTAP) after surface modification treatment for PDT deep tumor therapy. It was found that the energy transfer efficiency from ZnO nanoparticles to MTAP was as high as 83%. The ZnO-MTAP coupled system had lower cytotoxicity under dark conditions compared to single MTAP and ZnO. Later, Chen *et al.* further investigated the long afterglow properties of ZnS:Cu,Co NPS on this basis and compared the afterglow luminescence intensity at different Cu^{2+} and Co^{2+} doping concentrations.[30–33] It was found that the afterglow luminescence intensity of ZnS NPs excited by X-rays was the strongest when the Cu^{2+} doping concentration was 0.07% and the Co^{2+} doping concentration was 0.03%, showing efficient energy transfer efficiency and long-lasting afterglow properties. Even after the X-ray excitation is stopped, this afterglow can still be used as a long-lasting light source for PDT, which greatly reduces the dose and irradiation time of X-ray use. Moreover, ZnS:Cu,Co-TbRrh123 can kill nearly 60% of PC3 cells under 2 Gy X-ray irradiation, indicating that the composite system has good therapeutic effects.

Moreover, $ZnGa_2O_4$:Cr^{3+} (ZGC) is considered as a persistent luminescent material that avoids tissue autofluorescence interference, has a cubic spinel structure, can be excited by X-rays, and shows considerable promise for *in vivo* imaging and tumor therapy.[34–36] Shi *et al.*[37] reported that $Zn_3Ga_2GeO_8$:-Cr^{3+},Yb^{3+} with persistent luminescent properties. Er^{3+} NPs combined with mesoporous silicates as a novel nanotherapeutic agent for imaging and treatment of *in situ* liver tumors.[37]Monodisperse, uniform particle size

Open Access Article. Published on 16 October 2023. Downloaded on 8/7/2025 12:39:15 AM.
This article is licensed under a Creative Commons Attribution-NonCommercial 3.0 Unported Licence.

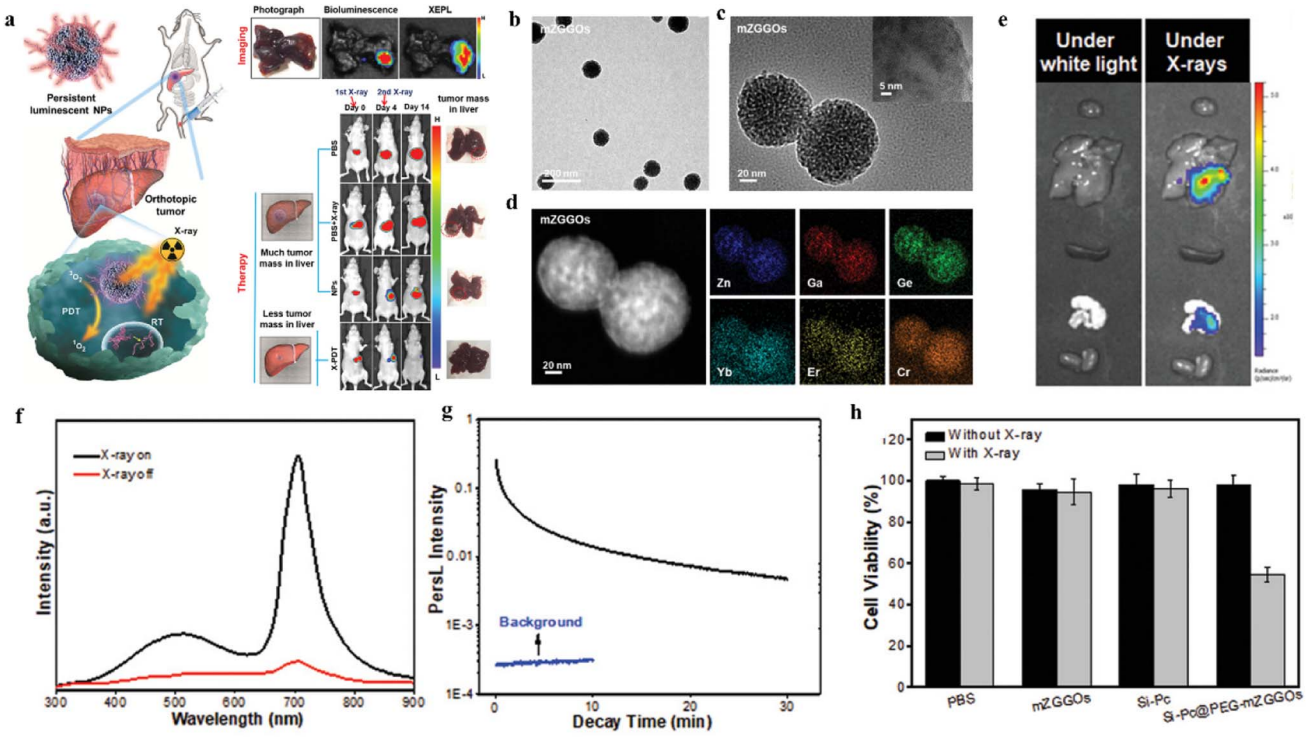

Fig. 8 Schematic diagram of (a) X-ray-induced sustained luminescence for ultrasensitive imaging and effective inhibition of *in situ* liver tumors; (b) TEM images of mZGGOs; (c) HR-TEM images of mZGGOs; (d) EDS elemental scan images of mZGGOs; (e) sustained luminescence imaging of isolated organs at 24 h after injection of Si-Pc@PEG-mZGGOs; (f) emission spectra of mZGGOs nanoparticles; (g) afterglow decay curves of mZGGOs after X-ray excitation; (h) HepG2 cell viability of PBS, ZGGO, Si-PC and Si-PC@PEG-mZGGOs after X-ray irradiation.[37]

$Zn_3Ga_2GeO_8$:Cr^{3+},Yb^{3+},Er^{3+} (mZGGOs) spherical nanoparticles were prepared by mesoporous silica template method. As shown in Fig. 8b–d, the nanoparticles have a size of about 100 nm, regular morphology, and uniform distribution of each constituent element. When the excitation of the X-ray light source was stopped, mZGGOs produced persistent luminescence in the near-infrared at 706 nm (as shown in Fig. 8f and g). The mechanism of persistent luminescence according to Cr^{3+}-doped $Zn_3Ga_2GeO_8$ suggests Cr^{3+} would generate a narrow-band emission (700 nm) due to the spin-forbidden $^2E \rightarrow {}^4A_2$ transition, or a broadband emission (650–1600 nm) due to the spin-allowed $^4T_2 \rightarrow {}^4A_2$ transition, which strongly depends on the environment of the host lattices. By loading silicon phthalocyanine (Si-PC) photosensitizer, mZGGOs can effectively excite the photosensitizer to produce $^1O_2$ to kill cancer cells by X-ray irradiation. Under the same conditions, the Si-PC@PEG-mZGGOs plus X-ray irradiation group showed a significant decrease in cell viability in the presence of X-ray irradiation compared with the PBS, mZGGOs and Si-PC groups (as in Fig. 8h), indicating that only fluorescence-mediated X-PDT could effectively induce HepG2 cell death. In Fig. 8e, Si-PC@PEG-mZGGOs nanoparticles were injected intravenously into *in situ* tumor-bearing mice, and a strong sustained luminescence signal was still detected in the isolated liver tumor region 24 hours after injection. Imaging of *in situ* liver tumors *in vivo* demonstrated that Si-PC@PEG-mZGGOs nanocomplexes could aggregate in liver tumors through a passive targeting mechanism. Under imaging guidance, X-PDT can effectively accumulate in the tumor region and inhibit the growth of *in situ* liver tumors *in vivo* with few side effects. Overall, X-ray induced sustained luminescence promotes ultrasensitive imaging and effective inhibition of *in situ* liver tumors.

2.3.3 Quantum dots. In recent years, quantum dot QDs (*e.g.*, CdTe, CdSe, *etc.*) have attracted a lot of attention from researchers due to their special optical properties, including strong absorbance and photothermal effects.[38] Due to the deep penetration depth of X-rays, it can be combined with QDs as a radiosensitizer to treat deep tumors by PDT. Yang *et al.*[39] reported a quantum dot (QDs) that can be excited with X-rays of MeV energy, consisting of a CdSe core and a ZnS shell layer with a particle size of only 2.1 nm (Fig. 9a). They are conjugated to the photosensitizer PhotoFrin by forming amide bonds to form QD–Photofrin complexes. Under X-ray irradiation at 6 MeV and 100–600 cGy min^{-1}, the number of visible photons produced by QDs was linearly related to the irradiation dose (Fig. 9c). The energy transfer from QDs to Photofrin is highly efficient and takes place *via* FRET. The efficiency of the FRET process also increases with the Photofrin/QD ratio. As shown in Fig. 9d, the emission of QDs was completely burst when the molar ratio reached 20 : 1. In the case of synthesis with a Photofrin/QD ratio of 291 : 1, the

 © 2023 The Author(s). Published by the Royal Society of Chemistry

Open Access Article. Published on 16 October 2023. Downloaded on 8/7/2025 12:39:15 AM.
This article is licensed under a Creative Commons Attribution-NonCommercial 3.0 Unported Licence.

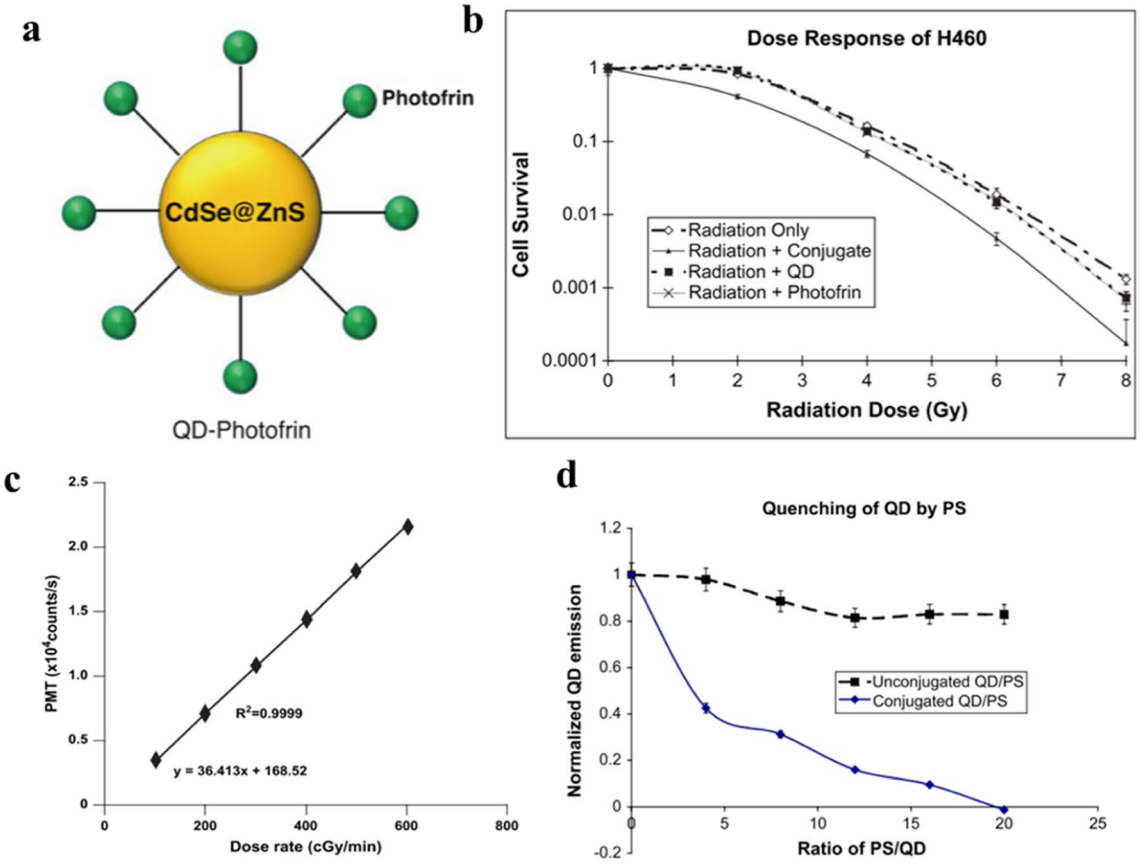

Fig. 9 (a) Structural diagram of QD–Photofrin; (b) H460 cell survival curve; (c) variation of the number of photons generated by quantum dots with irradiation dose rate; (d) luminescence properties of QD and QD–Photofrin under 6-MV X-ray irradiation.[39]

energy transfer efficiency is close to 100%. As shown in Fig. 9b, the combined X-ray/QD–PhotoFrin treatment enhanced H460 cell killing compared to irradiation alone. Therefore, this novel complex of quantum dots and photosensitizers is of great reference importance in clinical applications.

To address the problems of limited light penetration depth and lack of bacterial specificity of non-antibiotics, Pan *et al.* prepared a novel nanocarrier VAN-GQDS/PPIX complex.[40] As shown in Fig. 10a, the complex consists of graphene oxide quantum dots (GQDs), specific bacterial targeting ligands VAN and PPIX, and can be activated by X-rays with bacterial-specific toxicity. Among them, GQDs can carry bacterial targeting ligands (VAN) and radiosensitizers (PPIX) to increase the PPIX/VAN ratio in bacteria, thus reducing systemic toxicity, and also enhance X-ray induced PPIX to produce more reactive oxygen species and enhance bactericidal ability (Fig. 10b). In addition, the VAN-GQDS/PPIX complex showed even more sustained antibacterial effect for 7 days with at least 7 rounds of repeated dosing within a week (Fig. 10c). This study used a low dose of X-rays to effectively activate the VAN-GQDS/PPIX complex to exert its bactericidal effect on *E. coli* without causing damage to normal cells. These results suggest that the VAN-GQDS/PPIX complex is a suitable vehicle for X-ray triggering with specific toxicity against deep-seated bacteria.

3. Water-soluble modification of nanoparticle surface and loading strategy of photosensitizer

Despite the irreplaceable optical properties of luminescent nanoparticles for applications such as bioimaging and cancer therapy, their application in biomedical fields still faces many challenges. In particular, almost all high-performance and monodisperse NPs are currently synthesized from oleic acid or oleylamine ligands, which makes NPs unusable for most biomedical applications in aqueous environments.[41,42] Therefore, in order to be useful in practical applications, NPs need to be well dispersed in aqueous solutions, which requires water-soluble modification of their surfaces to give them hydrophilic properties. Some common water-soluble surfactants include EDTA, PEI, PAA, AEP, *etc.* Water-soluble modification of NPs by hydrothermal or solvothermal methods has been performed in the past, but their application in organisms is hindered by their large size. Nowadays, researchers have innovatively proposed the following methods to modify the original hydrophobic surface of NPs to make them better used in different biomedical fields. Commonly used methods are ligand surface engineering to improve the hydrophilicity of NPs, such as ligand removal, ligand exchange, and ligand oxidation. The surface can also be silylated or coated with amphiphilic polymers.

Open Access Article. Published on 16 October 2023. Downloaded on 8/7/2025 12:39:15 AM.
This article is licensed under a Creative Commons Attribution-NonCommercial 3.0 Unported Licence.

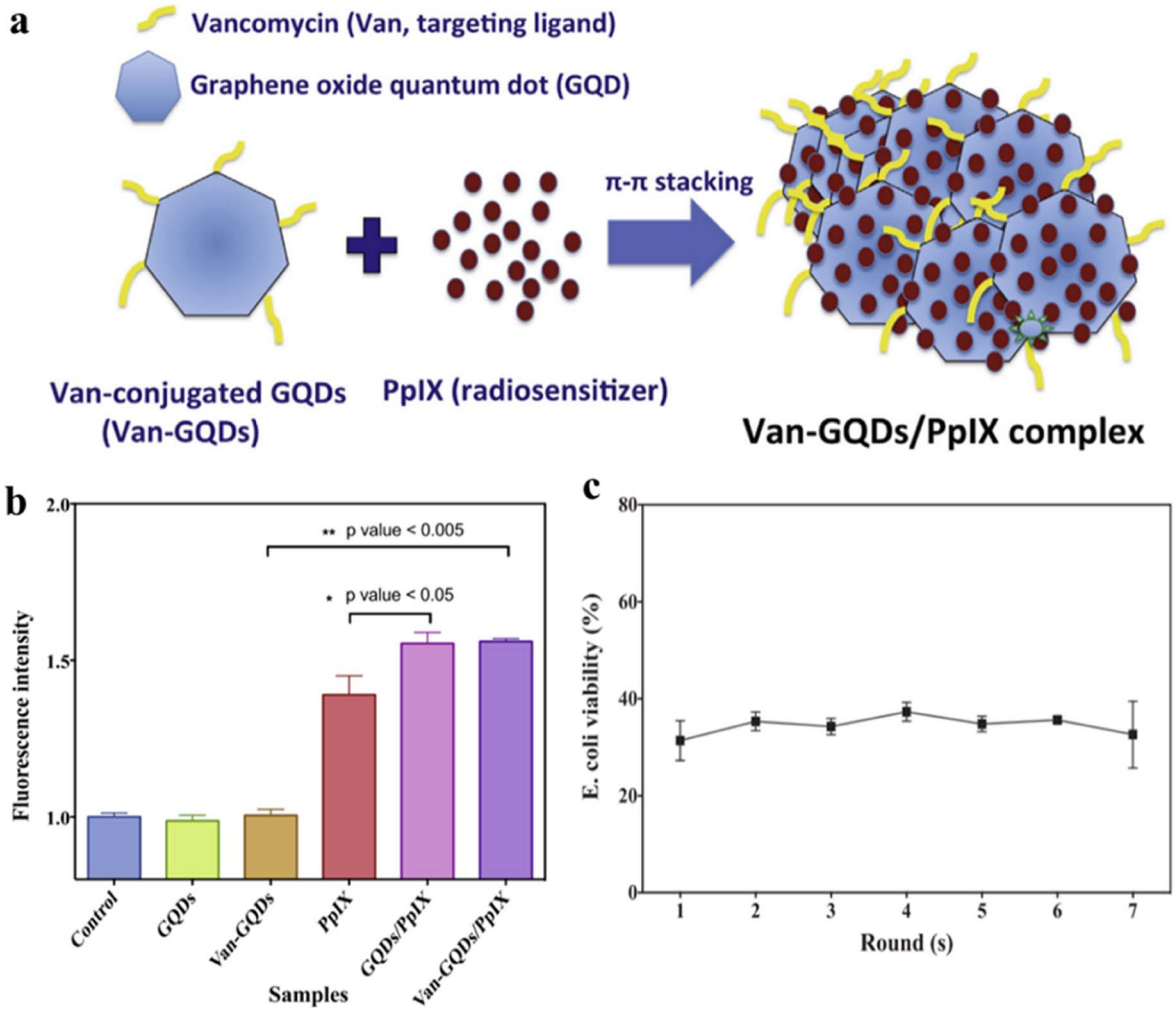

Fig. 10 (a) Preparation and structural composition of VAN-GQDS/PPIX complex; (b) extracellular reactive oxygen species content of different samples was determined by DPBF fluorescent probe; (c) sustained antibacterial effect of VAN-GQDS/PPIX complex against *E. coli* after 7 rounds of repeated administration and 24 h of X-ray irradiation.[40]

3.1 Water-soluble modification of nanoparticle surfaces

3.1.1 Ligand removal. For hydrophobic oleic acid ligand-covered NPs, direct removal of surface reagents is the simplest method for hydrophilic modification. As shown in Fig. 11a, there are two main routes: (1) acidic treatment of OA-covered NPs on the surface with 0.2 M HCl solution for about 2 h. Under acidic conditions (pH < 4), HCl can protonate the carboxylic acid group of OA, which leads to its removal from the surface of NPs, and ligand-free and water-dispersed NPs can be obtained.[43] (2) Substitution of OA with BF_4^- in sodium nitro tetrafluoroborate ($NOBF_4$) stabilizes NPs in various polar and hydrophilic media.[44] The ligand-free NPs prepared by these two methods can facilitate conjugation with hydrophilic biomolecules such as –COOH, $-SO_3H$, and $-PO_3H$, and these biomolecules are well coordinated to the lanthanide ions on the surface of the NPs.[45]

3.1.2 Ligand exchange. Ligand exchange is one of the most commonly used and effective methods in ligand engineering. As shown in Fig. 11b, two pathways are known to achieve ligand exchange, one in which the new ligand replaces the original ligand in one step; the other is a two-step substitution in which the OA is stripped by using $NOBF_4$ or treated with HCl in a strong acid method to produce ligand-free and water-dispersible particles. Then, it is re-covered with hydrophilic ligands. Various hydrophilic ligands, such as small molecules, polymers or macromolecules (citrate,[46] phosphate,[47] polyacrylic acid,[48] polyethyleneimine,[49] *etc.*) have been successfully used to modify the surface of NPs. For example, Satu Lahtinen *et al.*[50] removed OA from the surface of UCNPs by $NOBF_4$ ligand exchange and then incubated UCNPs in polyacrylic acid (PAA)/water solution to completely coat the surface with PAA to obtain highly dispersed nanoparticles for use in upconversion correlation spectroscopy (UCCS) homogeneous immunoassays of thyroid-promoting hormones. In UCCS measurements, the surface-modified UCNPs exhibited good dispersion even when plasma samples were used. And the efficiency of ligand exchange was improved by optimizing the particle size and shape of UCNPs. However, it was found that the luminescence intensity of almost all the NPs modified by small molecule

 © 2023 The Author(s). Published by the Royal Society of Chemistry

Open Access Article. Published on 16 October 2023. Downloaded on 8/7/2025 12:39:15 AM.
This article is licensed under a Creative Commons Attribution-NonCommercial 3.0 Unported Licence.

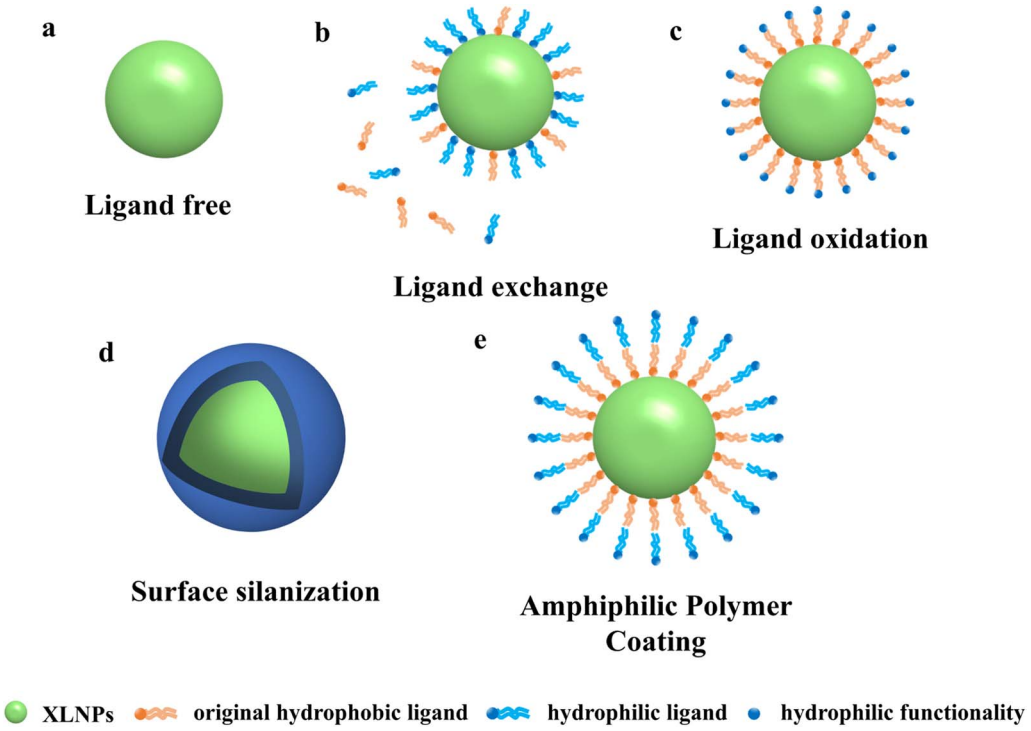

Fig. 11 Common methods for water-soluble modification of NPs surfaces: (a) ligand removal; (b) ligand exchange; (c) ligand oxidation; (d) surface silanization; (e) amphiphilic polymer coating.

ligands was dramatically reduced in aqueous solvents. In contrast, NPs coated with $NaYF_4$ did not show this phenomenon. However, the effect of small molecule coating on quantum yield and luminescence decay time has not been systematically investigated.

3.1.3 Ligand oxidation. Ligand oxidation is a simple but not universal method. The unsaturated carbon–carbon double bond of oleic acid or oleylamine is selectively generated into carboxyl or epoxy groups by using oxidizing agents. Common oxidants include Lemieux-von Rudloff reagent, ozone, *etc.*[51] The formation of reactive groups through ligand oxidation results in enhanced dispersion of NPs in water (Fig. 11c). Also, it is possible to conjugate with other therapeutic drugs on the surface of NPs to be able to accomplish drug delivery. Or conjugated with polyethylene glycol to improve their biocompatibility. However, since only ligands containing unsaturated carbon–carbon bonds can be oxidized. Therefore, the method of ligand oxidation is not universal.

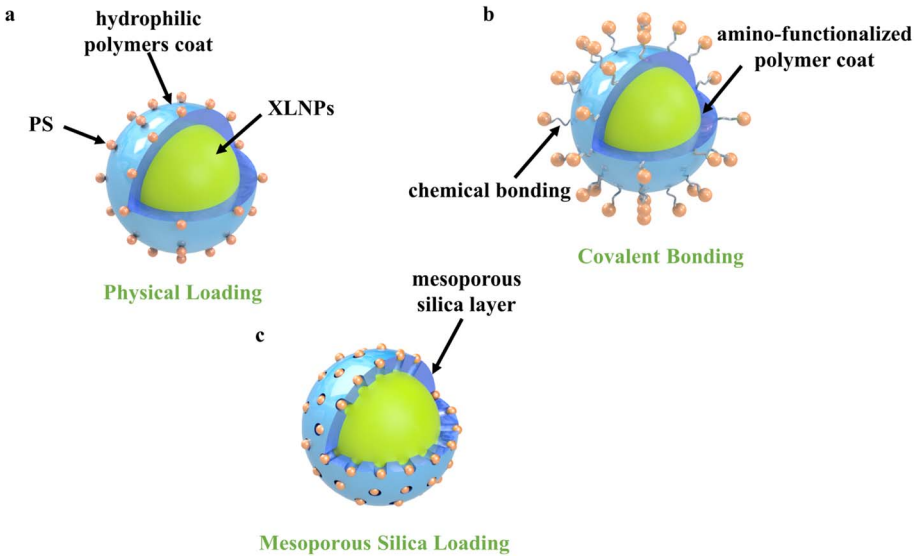

Fig. 12 Loading strategy of photosensitizer: (a) physical loading; (b) covalent bonding; (c) mesoporous silica loading.

Open Access Article. Published on 16 October 2023. Downloaded on 8/7/2025 12:39:15 AM.
This article is licensed under a Creative Commons Attribution-NonCommercial 3.0 Unported Licence.

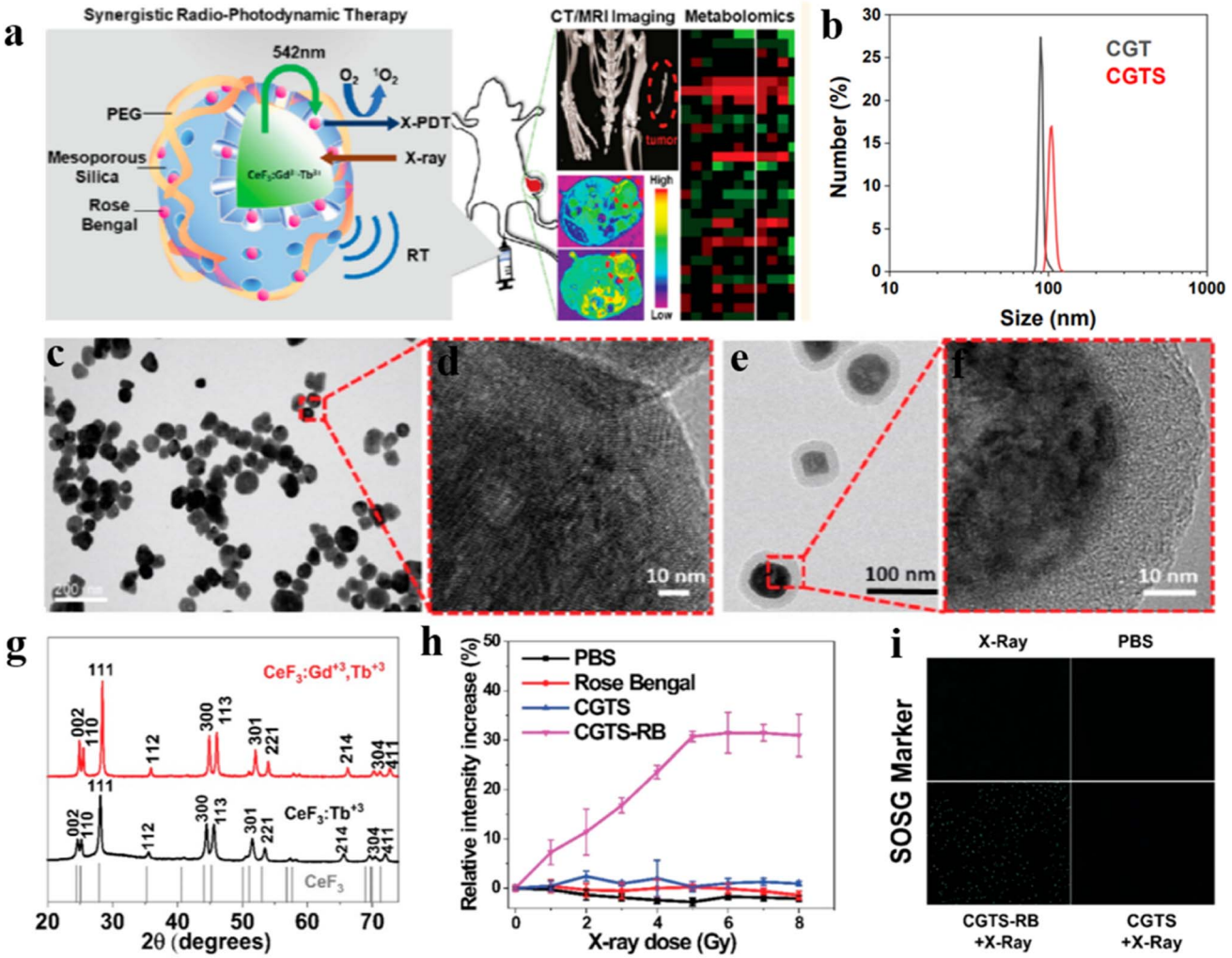

Fig. 13 (a) Schematic design strategy of CeF_3:Gd^{3+},Tb^{3+} NPs applied to X-PDT; (b) DLS analysis of the particle size distribution of CGT and CGTS nanoparticles in PBS; (c) morphology of CeF_3:Gd^{3+},Tb^{3+} NPs; (d) HRTEM image of CeF_3:Gd^{3+},Tb^{3+} NPs; (e) mesoporous silica-coated CeF_3:-Gd^{3+},Tb^{3+} NPs morphology; (f) HRTEM images of mesoporous silica-coated CeF_3:Gd^{3+},Tb^{3+} NPs; (g) XRD patterns of CeF_3:Gd^{3+},Tb^{3+} NPs and CeF_3:Tb^{3+} NPS; (h) SOSG method to measure single-linear state oxygen generation; (i) in 4T1 cell *in vitro* SOSG, after incubation of cells with CGTS-Rb NPs, X-ray irradiation resulted in effective intracellular generation of singlet oxygen, as evidenced by enhanced fluorescence.[67]

3.1.4 Surface silanization. Surface silanization is one of the most commonly used methods for water-soluble modification of hydrophilic NPs by hydrolysis and condensation of tetraethyl orthosilicate (TEOS) in a mixture of ethanol/water/ammonia. A thin silica shell is deposited on the surface of NPs (Fig. 11d). Silica is chemically stable, non-toxic and highly biocompatible, and its silanol-containing surface can be further modified by carboxyl groups, amino groups, *etc.*[52–54] In addition, the silica shell layer can avoid direct contact of NPs with the *in vivo* environment, reducing cytotoxicity and improving the stability of NPs.

3.1.5 Amphiphilic polymer coatings. In this approach, molecules containing hydrophobic long alkyl chains are coated on NPs containing OA on the surface, and since the OA-modified NPs are hydrophobic, the hydrophobic groups in the amphiphilic molecules form a stable bilayer structure with the hydrophobic OA layer through van der Waals interactions.[55] In which the hydrophilic groups point outward from the surface of the modified NPS and the hydrophobic tails are inserted between the oleate chains, ensuring the dispersion of the NPs in aqueous solutions (Fig. 11e). For example, S. J. Budijono *et al.*[56] in order to make rare earth ion doped $NaYF_4$:Yb^{3+}, Er^{3+} UCNPs stable and well dispersed in serum media. Two polymer surface modification methods for UCNPs were compared, one is direct ligand exchange of polyacrylic acid (PAA); the second one uses three block copolymers: poly(ethylene glycol)-*block*-poly-caprolactone (PEGB-PCL), poly(ethylene glycol)-*block*-poly(lactic acid)-poly(glycolic acid) (PEG-*b*-PLGA) and poly(ethylene glycol)-*block*-poly(lactic acid) (PEG-*b*-PLA) were coated on the surface of UCNPs to form a dense PEG layer. Both surface modification methods were found to disperse UCNPs in water, but the PEG surface-coated UCNPs exhibited better stability in buffer and serum media. This strategy of polymer modification of NPs provides strong support for bioimaging and photodynamic therapy.

 © 2023 The Author(s). Published by the Royal Society of Chemistry

Open Access Article. Published on 16 October 2023. Downloaded on 8/7/2025 12:39:15 AM.
This article is licensed under a Creative Commons Attribution-NonCommercial 3.0 Unported Licence.

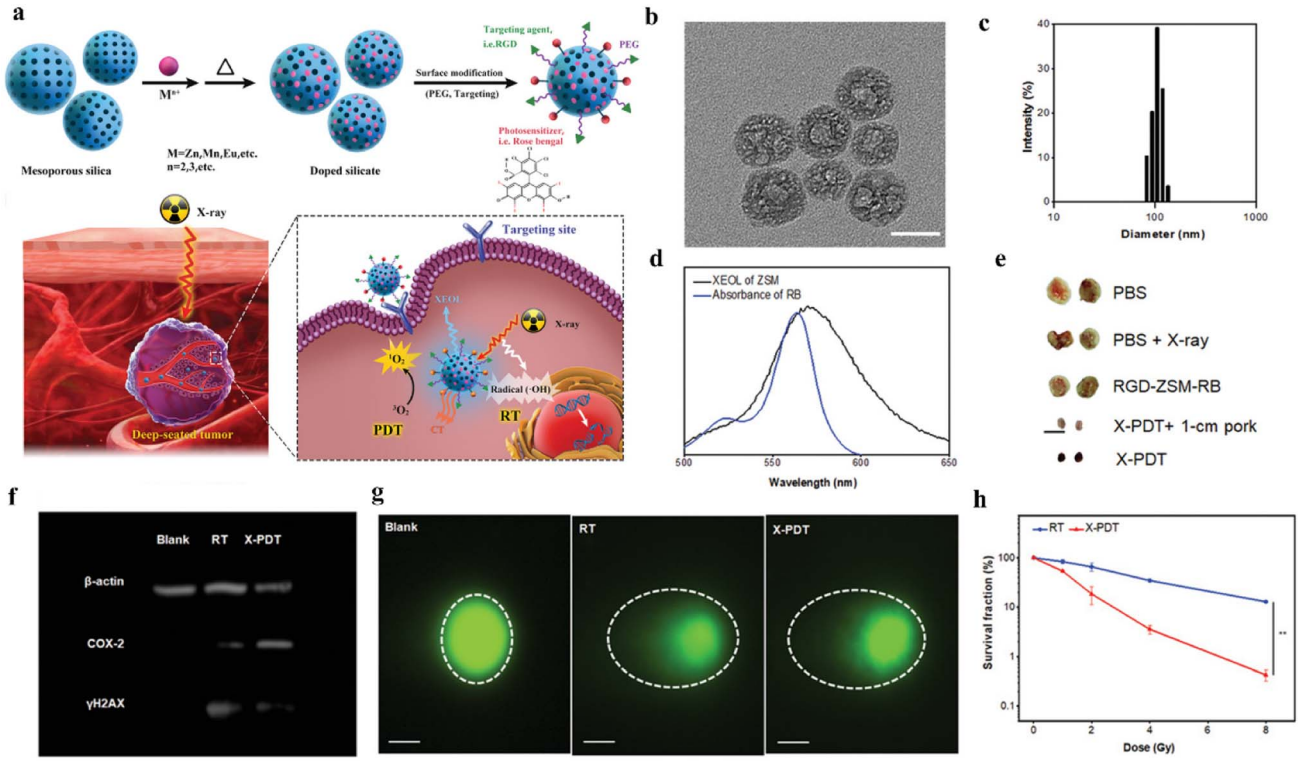

Fig. 14 (a) Schematic representation of the preparation process of RGD-ZSM-RB nanocoupled system and RGD-ZSM-RB mediated X-PDT mechanism; (b) TEM images of ZSM; (c) DLS analysis of the particle size distribution map of ZSM nanoparticles in water; (d) emission spectra of ZSM and absorption spectra of RB; (e) photographs of 5 different subgroups of tumors (scale bar 1 cm); (f) western blot analysis to demonstrate the effect of X-PDT on DNA and membrane lipids; (g) single-cell electrophoresis (scale bar, 25 μm) to assess DNA damage (dashed circles); (h) cell survival test after RT or X-PDT treatment.[68]

3.2 Loading strategy of photosensitizer

In order to achieve efficient X-PDT therapeutic effects, efficient energy transfer between X-ray excited nanoparticles and photosensitizers is essential. Conjugation of nanoparticles with photosensitizers by suitable loading means can significantly increase the FRET efficiency and thus improve the performance of nanocomplexes. To maximize FRET efficiency, in the accordance of FRET formula: $E = 1 - F_D/F_{DA}$, where F_D and F_{DA} are the corresponding luminescence intensities of the donors (XLNP) in the absence and presence of the acceptor (photosensitizer) at the same donor concentration, which is highly related to the distance between donors and acceptors, as well as spectrum matching of donors and acceptors. To minimize the distance between donors and acceptors, the surface modification strategy and photosensitizer conjugation strategies are essential.

3.2.1 Physical loading. The physical loading of photosensitizers generally relies on two pathways, namely polymer wrapping and electrostatic adherence.[57,58] Polymer wrapping is a way by which the photosensitizer molecules can be modified to the surface of the nano through interactions such as van der Waals forces between the photosensitizer and the polymer(Fig. 12a). Usually, nanoparticles are coated with a layer of hydrophobic oil solvent (*e.g.*, oleic acid, oleylamine, *etc.*) on the surface after synthesis to form a hydrophobic layer. The photosensitizer is adsorbed onto the nanoparticles by hydrophobic interactions, and then the surface is water-solubly modified and uniformly dispersed in the aqueous phase using hydrophilic polymers such as polyethyleneimine, PEG, chitosan, *etc.*[59] This method can adsorb more photosensitizer molecules and reduces the intermolecular distance between the photosensitizer and nanoparticles to improve the energy transfer efficiency. However, the concentration of loaded photosensitizer is too high and may also reduce the production of $^1O_2$.[60] Electrostatic adherence is achieved by using the interaction between molecules with opposite charges. However, this method is tedious and not easily controlled, and usually results in lower $^1O_2$ yields.

3.2.2 Covalent bonding. *In vivo* PDT therapy needs to be performed in a complex physiological microenvironment, which requires the prepared nanocomplexes to maintain their good stability *in vivo*. Therefore, a covalent bonding strategy was proposed, which utilizes the direct chemical bonding of groups in the photosensitizer (*e.g.*, carboxyl, amino, *etc.*) to functional groups on the nanoparticle surface.[61] This method ensures the stability of the photosensitizer on the nanoparticle surface, in addition to the bonding for PS, allows the attachment of some antibody fragments to enhance its targeting function. In addition, the covalent bonding has higher selectivity, enables the loading of a wide range of PSs, and can modulate the distance between NPs and PS molecules to improve the energy transfer

Open Access Article. Published on 16 October 2023. Downloaded on 8/7/2025 12:39:15 AM.
This article is licensed under a Creative Commons Attribution-NonCommercial 3.0 Unported Licence.

efficiency (Fig. 12b). However, its application is limited to *in vitro* studies because PS payloads achieved using covalent bonding are usually relatively small.

3.2.3 Mesoporous silica loading. Mesoporous silica has a porous structure with a high specific surface area (Fig. 12c), which can load more photosensitizer molecules by physical adsorption and can modulate the distance between nanoparticles and photosensitizers to achieve an efficient energy transfer system.[62,63] In addition, silica matrix has good biocompatibility and is often widely used as a drug carrier. However, the silica matrix is negatively charged, and the method is suitable for cationic and hydrophilic photosensitizer loading. And there is also a possibility that the photosensitizer may leak out of the pores during *in vivo* PDT treatment, which affects the therapeutic effect.

4. Treatment effect of X-PDT

X-PDT is an emerging strategy for the treatment of cancer, using highly penetrating X-rays as an external excitation source instead of traditional UV or visible light excitation, capable of treating deep tumors, and is a highly specific, non-invasive treatment. This treatment is safer and has fewer side effects on normal tissues than chemotherapy (CT) and radiotherapy (RT), which are based on the mechanism of using high-energy X-rays/gamma photons that act directly on DNA to destroy its biological structure and the reaction of photons or electrons with H_2O to produce $-O_2$ or –OH to kill tumor cells.[64–66] However, to achieve a better therapeutic effect it is necessary to use high doses of X-ray radiation (about 45–60 Gy), which can cause damage to the normal tissues of the body. X-PDT uses scintillation nanoparticles as an energy conversion medium to transfer the absorbed X-ray energy to the photosensitizer to generate reactive oxygen species for therapeutic purposes. It greatly reduces the irradiation dose of X-rays compared to RT and has great clinical potential for the treatment of deep-seated tumors.

Farooq Ahmad *et al.*[67] reported the synthesis of Gd^{3+}, Tb^{3+} co-doped CeF_3 NPs using hydrothermal method with higher luminescence efficiency compared to Tb^{3+} alone. As shown in Fig. 13a, by coating mesoporous silica on the surface of CeF_3:Gd^{3+}, Tb^{3+} scintillation nanoparticles and carrying a photosensitizer Rose Bengal to form a coupling system (CGTS-RB), a large amount of $^1O_2$ can be produced under X-ray excitation. In Fig. 13b–d, dynamic light scattering (DLS) and TEM show that CeF_3:Gd^{3+}. Tb^{3+} NPs with a particle size of about 80 nm and clear lattice stripes. In contrast, TEM and HRTEM images using mesoporous silica coated CGTs NPs (*e.g.*, Fig. 13e and f) can be observed to have regular and uniformly distributed morphology with an average size of about 91 nm. As shown in Fig. 13g, the XRD patterns of CeF_3:Gd^{3+}, Tb^{3+} NPS and CeF_3:Tb^{3+} NPs are all similar to those of standard CeF_3 crystals (JCPDS: 08-0045) hexagonal phase structure with the characteristic peaks matching. Fig. 13h shows the variation of $^1O_2$ content measured using singlet oxygen sensor (SOSG) analysis. After controlled experiments it was found that $^1O_2$ could not be

Table 1 Luminous nanoparticles for use in X-PDT

Nanoparticles	Size (nm)	Emission wavelength (nm)	Synthesis methods	Photosensitizers	Absorption wavelength (nm)	Attachment strategy	Ref.
LaF_3:Tb^{3+}	15	450–600	Hydrothermal method	Photofrin	400–500	Covalent binding	7
LaF_3:Tb^{3+}	25–50	450–600	Hydrothermal method	RB	450–600	Covalent binding	25
LaF_3:Tb^{3+}	15–50	450–600	Hydrothermal method	RB	450–600	Physical loading	26
LaF_3:Ce^{3+}	2 μm	500–600	Wet chemical method	PPIX	350–450	Physical loading	69
CeF_3	7–11	300–450	Coprecipitation method	Verteporfin	350–450	Physical loading	70
$LiYF_4$:Ce^{3+}	34	300–350	Thermal decomposition	ZnO	250–350	Covalent binding	71
$NaGdF_4$:Eu^{3+}	245	750–850	Hydrothermal method	Indocyanine green	750–850	Silica loading	72
$NaGdF_4$:15% Tb^{3+}	9	525–575	Coprecipitation method	RB	450–600	Covalent binding	73
Tb_2O_3	10	450–650	N/A	Photofrin	400–500	Silica loading	74
Y_2O_3	12	300–500	N/A	Psoralen	250–350	Covalent binding	75
ZnS:Cu,Co	4	450–550	Wet chemical method	TBrRh-123	500–550	Physical loading	76
Gd_2O_2S:Tb	20 μm	450–700	N/A	Photofrin II	400–600	N/A	77
$LiGa_5O_8$:Cr	100	700–750	sol–gel process	Naphthalocyanine	750–850	Silica loading	78
$ZnGa_2O_4$:Cr	15	650–750	Thermal decomposition	ZnPcS4	600–700	Physical loading	34
$Zn_3Ga_2GeO_8$:Cr^{3+},Yb^{3+},Er^{3+}	100	600–800	Mesoporous silica template method	Silica phthalocyanine	650–750	Silica loading	37
Cu-Cy	200	600–700	Wet chemical method	Cu-Cy	600–700	N/A	79
$SrAl_2O_4$:Eu@SiO_2	400	450–600	Vapour deposition	MC540	500–600	Silica loading	29
$Gd_2(WO_4)_3$:Tb	50	500–600	Hydrothermal method	MC540	500–600	Covalent binding	80

 © 2023 The Author(s). Published by the Royal Society of Chemistry

Open Access Article. Published on 16 October 2023. Downloaded on 8/7/2025 12:39:15 AM.
This article is licensed under a Creative Commons Attribution-NonCommercial 3.0 Unported Licence.

produced with X-ray, PBS, RB and CGTS NPs only. $^1O_2$ was produced only when CGTS-RB NPs and X-ray were used together and it was concluded that $^1O_2$ production was positively correlated with the X-ray irradiation dose. $^1O_2$ production was also detected in 4T1 cells *in vitro* (as in Fig. 13i), and green fluorescence was observed in the RT + XPDT (CGTS-RB + X-ray) group, indicating significant intracellular $^1O_2$ production. No significant increase in SOSG signal was observed when either CGTS + X-ray or single X-ray irradiated 4T1 cells, confirming that the synergistic RT + XPDT treatment mode relative to single RT with more significant tumor suppression effects, and also proposed the use of synergistic RT + XPDT treatment modality in combination with non-targeted global metabolomics.

The X-PDT strategy has proven its feasibility in clinical practice over the years since it was first proposed, especially in terms of being able to maintain high therapeutic efficiency using low doses of radiation. We found that in recent years, research has focused on the use of lower doses of X-PDT, and that a deeper understanding of the mechanism of action of X-PDT and the clever design of nanoscintillator–photosensitizer coupling systems are required to reduce the dose of X-rays used. Encouragingly, some researchers have already achieved promising results through ingenious designs. For example, Sun *et al.*[68] used a silica template method to synthesize biocompatible silicate nanoscintillators with uniform size and controllable particle size on a large scale, as shown in Fig. 14a. Zn- and Mn-doped silicate (ZSM) nanoparticles with a particle size of 101.2 ± 2.7 nm were synthesized by regulating the doping amounts of metals Zn and Mn using the silica template method (Fig. 14b and c) and produced emission spectra from 450 to 900 nm under X-ray excitation. The ZSM particles were then water-soluble modified on their surface with biocompatible polymers (PEG), and the ZSM particles were conjugated with targeted cyclic arginylglycyl aspartate (RGD) peptides and photosensitizers (RB) for X-ray imaging and targeted therapy, which enhanced the therapeutic effect of PDT. As shown in Fig. 14d, under X-ray irradiation, the ZSM nanoparticles emitted a strong peak located at 570 nm with a good overlap with the absorption spectrum of Rb, which improved the FRET efficiency. Fig. 14f and g shows the western blot analysis as well as single cell electrophoresis tests, which revealed a high frequency of strand breaks leading to enhanced DNA damage. *In vitro* and *in vivo* experiments showed that RGD-ZSM-RB could be effectively enriched in tumor cells and showed good *in vivo* deep tumor treatment under low dose X-ray (50 kV, 1.0 Gy) irradiation (Fig. 14e). This method provides a new idea for the synthesis of controllable luminescent nanoparticles to achieve low-dose X-PDT.

5. Conclusions and future outlook

This review summarizes the research progress of X-PDT in recent years and discuss two aspects, namely, the material selection of X-ray excited luminescent nanoparticles and the therapeutic effect of X-PDT. In terms of material selection, we present in detail the mechanism of action of X-PDT and the principle of luminescent nanoparticles in PDT. Different types of luminescent nanomaterials and luminescence enhancement strategies are listed. Several different methods of photosensitizer loading are compared to provide new ideas for achieving efficient FRET. In addition, different types of nanoparticle surface water-soluble modifications are presented, aiming to improve their dispersion and biocompatibility in aqueous solutions. Regarding the therapeutic effect of X-PDT, it was found that X-PDT has the advantages of high penetration, non-invasiveness and selectivity by comparing with RT. Moreover, it can produce better therapeutic effects under low-dose X-ray irradiation and can produce effective inhibition of deep-seated tumors. However, although X-PDT has achieved remarkable results so far, there is still a big gap for clinical applications. This is partly due to the low indexes of the X-PDT system in terms of $^1O_2$ yield, tumor cell destruction efficiency and tumor suppression ability. Table 1 summarizes a variety of scintillation nanoparticles used in X-PDT in recent years, and there is still room for improving the luminescence efficiency of nanoparticles and the FRET efficiency with photosensitizers. Specific improvements should be made in the following aspects.

(1) The luminescence efficiency and luminescence time of luminescent nanoparticles need to be improved urgently. Improving their luminescence intensity and lengthening the luminescence time not only can activate the photosensitizer more effectively and improve the PDT efficiency, but also can reduce the dose of X-ray use and have a lower signal-to-noise ratio and clearer imaging in biological imaging. Usually nanoparticles with high density and high atomic number have stronger X-ray absorption ability and tend to produce stronger luminescent radiation. However, it is worth noting that the luminescence intensity of nanoparticles is highly dependent on both their particle size and dispersion. Most of the current luminescent materials are still bulk materials. Therefore, it is crucial to obtain nanoparticles with smaller size and uniform distribution by improving the preparation process. And prolonging the luminescence time can be achieved by doping ions to introduce defects, increasing the concentration of traps, trapping more electrons and then releasing them slowly to achieve sustained luminescence.

(2) To elucidate the potential mechanism between the incident X-ray photon energy and the energy band structure of luminescent nanoparticles, as well as to determine the optimal excitation energy range. However, in most of the current research works, no definite conclusion has been reached yet.

(3) The FRET efficiency between nanoparticles and photosensitizers directly affects the yield of ROS. The FRET efficiency mainly depends on the degree of spectral overlap between the two and the intermolecular distance. Therefore, the selection of spectrally matched nanoparticles and photosensitizers, the design of assembly strategies and the selection of suitable loading methods to control the distance between them are the keys to solve this problem.

(4) Beside of the ROS generation of XLNP/PS nanocomplex improvements, current delivery strategy of XLNP/PS is intratumor injection; however, aiming for the clinical application in the future, the XLNP/PS nanocomplex should be delivered to the

Open Access Article. Published on 16 October 2023. Downloaded on 8/7/2025 12:39:15 AM.
This article is licensed under a Creative Commons Attribution-NonCommercial 3.0 Unported Licence.

tumor site with blood circulation. Thus, the tumor targeting function, long blood circulation time and minimal non-specific absorption by liver need to be consider with care, which are mainly depending on the surface modification strategies, such as PEGylation and target molecule conjugation.

In conclusion, X-PDT still has great potential for development and research prospects. We also believe that in the future, with the continuous development in the fields of material science, nanotechnology and biomedicine, X-PDT with low radiation dose is expected to become an effective and feasible technology in cancer treatment.

Conflicts of interest

There are no conflicts to declare.

References

1 W. P. Fan, P. Huang and X. Y. Chen, *Chem. Soc. Rev.*, 2016, **45**(23), 6488.
2 T. J. Dougherty, J. E. Kaufman, A. Goldfarb, K. R. Weishaupt, D. Boyle and A. Mittleman, *Cancer Res.*, 1978, **38**(8), 2628.
3 T. J. Dougherty, C. J. Gomer, B. W. Henderson, G. Jori, D. Kessel, M. Korbelik, J. Moan and Q. Peng, Photodynamic Therapy, *J. Natl. Cancer Inst.*, 1998, **90**, 889–905.
4 M. C. DeRosa and R. J. Crutchley, Photosensitized Singlet Oxygen and Its Applications, *Coord. Chem. Rev.*, 2002, **233**, 351–371.
5 M. Ethirajan, Y. Chen, P. Joshi and R. K. Pandey, The Role of Porphyrin Chemistry in Tumor Imaging and Photodynamic Therapy, *Chem. Soc. Rev.*, 2011, **40**, 340–362.
6 A. M. Smith, M. C. Mancini and S. Nie, Bioimaging: Second Window for in Vivo Imaging, *Nat. Nanotechnol.*, 2009, **4**, 710–711.
7 W. Chen and J. Zhang, Using Nanoparticles to Enable Simultaneous Radiation and Photodynamic Therapies for Cancer Treatment, *J. Nanosci. Nanotechnol.*, 2006, **6**, 1159–1166.
8 J. Q. Grim, Q. Li, K. B. Ucer, A. Burger, G. A. Bizarri, W. W. Moses and R. T. Williams, *Phys. Status Solidi A*, 2012, **209**, 2421.
9 W. Chen, Nanoparticle self-lighting photodynamic therapy for cancer treatment, *J. Biomed. Nanotechnol.*, 2008, **4**, 369–376.
10 S. Sindhwani, A. M. Syed and J. Ngai, The Entry of Nanoparticles into Solid Tumours, *Nat. Mater.*, 2020, **19**, 566–575.
11 A. C. Anselmo and S. Mitragotri, Nanoparticles in the Clinic: An Update, *Bioeng. Transl. Med.*, 2019, **4**, e10143.
12 C. Louis, R. Bazzi, C. A. Marquette, J. L. Bridot, S. Ledoux and B. Mercier, *Chem. Mater.*, 2005, **17**(7), 1673.
13 D. J. Naczynski, C. Sun, S. Türkcan, C. Jenkins, A. L. Koh, D. Ikeda, G. Pratx and L. Xing, *Nano Lett.*, 2015, **15**(1), 96.
14 D. E. Dolmans, D. Fukumura and R. K. Jain, Photodynamic Therapy for Cancer, *Nat. Rev. Cancer*, 2003, **3**, 380–387.
15 J. Moan and K. Berg, The Photodegradation of Porphyrins in Cells Can Be Used to Estimate the Lifetime of Singlet Oxygen, *Photochem. Photobiol.*, 1991, **53**, 549–553.
16 G. Blasse, Scintillator Materials, *Chem. Mater.*, 1994, **6**, 1465–1475.
17 S. S. Lucky, K. C. Soo and Y. Zhang, Nanoparticles in Photodynamic Therapy, *Chem. Rev.*, 2015, **115**, 1990–2042.
18 J. Hu, Y. Tang, A. H. Elmenoufy, H. Xu, Z. Cheng and X. Yang, Nanocomposite-Based Photodynamic Therapy Strategies for Deep Tumor Treatment, *Small*, 2015, **11**, 5860–5887.
19 H. Lusic and M. W. Grinstaff, X-Ray-Computed Tomography Contrast Agents, *Chem. Rev.*, 2013, **113**, 1641–1666.
20 C. Sun, G. Pratx, C. M. Carpenter, H. G. Liu, Z. Cheng, S. S. Gambhir and L. Xing, *Adv. Mater.*, 2011, **23**(24), H195.
21 K. W. Kramer, D. Biner, G. Frei, H. U. Gdel, M. P. Hehlen and S. R. Luthi, *Chem. Mater.*, 2004, **16**, 1244.
22 A. Aebischer, M. Hostettler, J. Hauser, K. Krmer, T. Weber, H.-U. Gdel and H.-B. Brgi, *Angew. Chem.*, 2006, **118**, 2869; *Angew. Chem., Int. Ed.*, 2006, **45**, 2802.
23 A. Aebischer, S. Heer, D. Biner, K. Krmer, M. Haase and H. U. Gdel, *Chem. Phys. Lett.*, 2005, **407**, 124.
24 B. Liu, C. Li, P. Yang, Z. Hou and J. Lin, 808-nm-Light-excited lanthanide-doped nanoparticles: rational design, luminescence control and theranostic applications, *Adv. Mater.*, 2017, **29**, 1605434.
25 Y. F. Liu, W. Chen, S. P. Wang, A. G. Joly, S. Westcott and B. K. Woo, *J. Appl. Phys.*, 2008, **103**(6), 063105.
26 Y. A. Tang, J. Hu, A. H. Elmenoufy and X. L. Yang, *ACS Appl. Mater. Interfaces*, 2015, **7**(22), 12261.
27 Y. Liu, *et al.*, Significantly enhanced afterglow brightness via intramo-lecular energy transfer, *ACS Mater. Lett.*, 2021, **3**, 713–720.
28 X. Ou, *et al.*, High-resolution X-ray luminescence extension imaging, *Nature*, 2021, **590**, 410–415.
29 H. M. Chen, G. D. Wang, Y. J. Chuang, Z. P. Zhen, X. Y. Chen, P. Biddinger, Z. L. Hao, F. Liu, B. Z. Shen, Z. W. Pan and J. Xie, *Nano Lett.*, 2015, **15**(4), 2249.
30 L. Ma and W. Chen, *Nanotechnology*, 2010, **21**(38), 385604.
31 L. Ma and W. Chen, *J. Phys. Chem. C*, 2011, **115**(18), 8940.
32 L. Ma, X. J. Zou, B. Bui, W. Chen, K. H. Song and T. Solberg, *Appl. Phys. Lett.*, 2014, **105**(1), 013702.
33 L. Ma, X. J. Zou, M. Hossu and W. Chen, *Nanotechnology*, 2016, **27**(31), 315602.
34 T. Maldiney, A. Bessière, J. Seguin, E. Teston, S. K. Sharma, B. Viana, A. J. J. Bos, P. Dorenbos, M. Bessodes, D. Gourier, D. Scherman and C. Richard, *Nat. Mater.*, 2014, **13**, 418.
35 Z. Li, Y. Zhang, X. Wu, L. Huang, D. Li, W. Fan and G. Han, *J. Am. Chem. Soc.*, 2015, **137**, 5304.
36 J. Wang, Q. Ma, X. X. Hu, H. Liu, W. Zheng, X. Chen, Q. Yuan and W. Tan, *ACS Nano*, 2017, **11**, 8010.
37 T. Shi, W. Sun, R. Qin, *et al.*, X-ray-induced persistent luminescence promotes ultrasensitive imaging and effective inhibition of orthotopic hepatic tumors, *Adv. Funct. Mater.*, 2020, **30**(24), 2001166.

 © 2023 The Author(s). Published by the Royal Society of Chemistry

Open Access Article. Published on 16 October 2023. Downloaded on 8/7/2025 12:39:15 AM.
This article is licensed under a Creative Commons Attribution-NonCommercial 3.0 Unported Licence.

38 J. Takahashi and M. Misawa, Analysis of potential radiosensitizing materials for X-ray-induced photodynamic therapy, *NanoBiotechnology*, 2007, **3**, 116–126.
39 W. Yang, P. W. Read, J. Mi, *et al.*, Semiconductor nanoparticles as energy mediators for photosensitizer-enhanced radiotherapy, *Int. J. Radiat. Oncol., Biol., Phys.*, 2008, **72**(3), 633–635.
40 C. L. Pan, M. H. Chen, F. I. Tung, *et al.*, A nanovehicle developed for treating deep-seated bacteria using low-dose X-ray, *Acta Biomater.*, 2017, **47**, 159–169.
41 H. Oliveira, A. Bednarkiewicz, A. Falk, E. Frohlich, D. Lisjak, A. Prina-Mello, S. Resch, C. Schimpel, I. V. Vrcek, E. Wysokinska and H. H. Gorris, *Adv. Healthcare Mater.*, 2019, **8**, 1801233.
42 S. Wilhelm, M. Kaiser, C. Wurth, J. Heiland, C. Carrillo-Carrion, V. Muhr, O. S. Wolfbeis, W. J. Parak, U. Resch-Genger and T. Hirsch, *Nanoscale*, 2015, **7**, 1403.
43 N. Bogdan, F. Vetrone, G. A. Ozin and J. A. Capobianco, *Nano Lett.*, 2011, **11**, 835.
44 A. Dong, X. Ye, J. Chen, Y. Kang, T. Gordon, J. M. Kikkawa and C. B. Murray, *J. Am. Chem. Soc.*, 2011, **133**, 998.
45 H. T. T. Duong, Y. H. Chen, S. A. Tawfik, S. H. Wen, M. Parviz, O. Shimoni and D. Y. Jin, *RSC Adv.*, 2018, **8**, 4842.
46 R. Naccache, P. Chevallier, J. Lagueux, Y. Gossuin, S. Laurent, L. Vander Elst, C. Chilian, J. A. Capobianco and M. A. Fortin, *Adv. Healthcare Mater.*, 2013, **2**, 1478.
47 A. Nsubuga, M. Sgarzi, K. Zarschler, M. Kubeil, R. Hubner, R. Steudtner, B. Graham, T. Joshi and H. Stephan, *Dalton Trans.*, 2018, **47**, 8595.
48 S. Lahtinen, M. B. Liisberg, K. Raiko, S. Krause, T. Soukka and T. Vosch, *ACS Appl. Nano Mater.*, 2021, **4**, 432.
49 A. E. Guller, A. Nadort, A. N. Generalova, E. V. Khaydukov, A. V. Nechaev, I. A. Kornienko, E. V. Petersen, L. Liang, A. B. Shekhter, Y. Qian, E. M. Goldys and A. V. Zvyagin, *ACS Biomater. Sci. Eng.*, 2018, **4**, 3143.
50 S. Lahtinen, M. Baldtzer Liisberg, K. Raiko, *et al.*, Thulium- and Erbium-Doped Nanoparticles with Poly (acrylic acid) Coating for upconversion cross-correlation spectroscopy-based sandwich immunoassays in plasma, *ACS Appl. Nano Mater.*, 2020, **4**(1), 432–440.
51 Z. Chen, H. Chen, H. Hu, M. Yu, F. Li, Q. Zhang, Z. Zhou, T. Yi and C. Huang, Versatile Synthesis Strategy for Carboxylic Acid-functionalized Upconverting Nanophosphors as Biological Labels, *J. Am. Chem. Soc.*, 2008, **130**, 3023–3029.
52 A. Guerrero-Martinez, J. Perez-Juste and L. M. Liz-Marzan, *Adv. Mater.*, 2010, **22**, 1182.
53 K. Osseo-Asare and F. J. Arriagada, *Colloids Surf.*, 1990, **50**, 321.
54 C. Kembuan, M. Saleh, B. Ruhle, U. Resch-Genger and C. Graf, *Beilstein J. Nanotechnol.*, 2019, **10**, 2410.
55 V. Muhr, S. Wilhelm, T. Hirsch and O. S. Wolfbeis, *Acc. Chem. Res.*, 2014, **47**, 3481.
56 S. J. Budijono, J. Shan, N. Yao, *et al.*, Synthesis of stable block-copolymer-protected NaYF4: Yb3+, Er3+ up-converting phosphor nanoparticles, *Chem. Mater.*, 2010, **22**(2), 311–318.
57 Q. Yuan, Y. Wu, J. Wang, D. Lu, Z. Zhao, T. Liu, X. Zhang and W. Tan, Targeted Bioimaging and Photodynamic Therapy Nanoplat-form Using an Aptamer-Guided G-Quadruplex DNA Carrier and near-Infrared Light, *Angew. Chem., Int. Ed.*, 2013, **52**, 13965–13969.
58 Z. Yu, Q. Sun, W. Pan, N. Li and B. Tang, A Near-Infrared Triggered Nanophotosensitizer Inducing Domino Effect on Mitochon-drial Reactive Oxygen Species Burst for Cancer Therapy, *ACS Nano*, 2015, **9**, 11064–11074.
59 X. Zou, M. Yao, L. Ma, M. Hossu, X. Han, P. Juzenas and W. Chen, X-Ray-Induced Nanoparticle-Based Photodynamic Therapy of Cancer, *Nanomedicine*, 2014, **9**, 2339–2351.
60 N. A. Kuznetsova, N. S. Gretsova, V. M. Derkacheva, O. L. Kaliya and E. A. Lukyanets, Sulfonated Phthalocyanines: Aggregation and Singlet Oxygen Quantum Yield in Aqueous Solutions, *J. Porphyrins Phthalocyanines*, 2003, **7**, 147–154.
61 A. Kamkaew, F. Chen, Y. Zhan, *et al.*, Nanopartículas centelleantes como mediadores de energía para una terapia fotodinámica mejorada, *ACS Nano*, 2016, **10**(4), 3918–3935.
62 N. M. Idris, M. K. Gnanasammandhan, J. Zhang, P. C. Ho, R. Mahendran and Y. Zhang, In Vivo Photodynamic Therapy Using Upconversion Nanoparticles as Remote-Controlled Nanotransducers, *Nat. Med.*, 2012, **18**, 1580–1585.
63 P. Yang, S. Gai and J. Lin, Functionalized Mesoporous Silica Materials for Controlled Drug Delivery, *Chem. Soc. Rev.*, 2012, **41**, 3679–3698.
64 X. Li, J. F. Lovell, J. Yoon and X. Chen, Clinical Development and Potential of Photothermal and Photodynamic Therapies for Cancer, *Nat. Rev. Clin. Oncol.*, 2020, **17**, 657–674.
65 S. A. McFarland, A. Mandel, R. Dumoulin-White and G. Gasser, Metal-Based Photosensitizers for Photodynamic Therapy: The Future of Multimodal Oncology?, *Curr. Opin. Chem. Biol.*, 2020, **56**, 23–27.
66 P. C. A. Swamy, G. Sivaraman, R. N. Priyanka, S. O. Raja, K. Ponnuvel, J. Shanmugpriya and A. Gulyani, Near Infrared (NIR) Absorbing Dyes as Promising Photosensitizer for Photo Dynamic Therapy, *Coord. Chem. Rev.*, 2020, **411**, 213233.
67 F. Ahmad, X. Wang, Z. Jiang, *et al.*, Codoping enhanced radioluminescence of nanoscintillators for X-ray-activated synergistic cancer therapy and prognosis using metabolomics, *ACS Nano*, 2019, **13**(9), 10419–10433.
68 W. Sun, T. Shi, L. Luo, *et al.*, Monodisperse and uniform mesoporous silicate nanosensitizers achieve low-dose X-ray-induced deep-penetrating photodynamic therapy, *Adv. Mater.*, 2019, **31**(16), 1808024.
69 X. Zou, *et al.*, X-ray-induced nanoparticle-based photodynamic therapy of cancer, *Nanomedicine*, 2014, **9**(15), 2339–2351.
70 S. Clement, *et al.*, X-ray induced singlet oxygen generation by nanoparticle-photosensitizer conjugates for photodynamic therapy: determination of singlet oxygen quantum yield, *Sci. Rep.*, 2016, **6**, 19954.

Open Access Article. Published on 16 October 2023. Downloaded on 8/7/2025 12:39:15 AM.
This article is licensed under a Creative Commons Attribution-NonCommercial 3.0 Unported Licence.

71 C. Zhang, *et al.*, Marriage of Scintillator and Semiconductor for Synchronous Radiotherapy and Deep Photodynamic Therapy with Diminished Oxygen Dependence, *Angew. Chem.*, 2015, **127**(6), 1790–1794.

72 Y. Dou, Y. Liu, F. Zhao, *et al.*, Radiation-responsive scintillating nanotheranostics for reduced hypoxic radioresistance under ROS/NO-mediated tumor microenvironment regulation, *Theranostics*, 2018, **8**(21), 5870.

73 W. Zhang, *et al.*, Ultra-high FRET efficiency NaGdF4: Tb3+-Rose Bengal biocompatible nanocomposite for X-ray excited photodynamic therapy application, *Biomaterials*, 2018, **184**, 31–40.

74 A. Bulin, *et al.*, X-ray-induced singlet oxygen activation with nanoscintillator-coupled porphyrins, *J. Phys. Chem. C*, 2013, **117**(41), 21583–21589.

75 J. P. Scaffidi, *et al.*, Activity of psoralen-functionalized nanoscintillators against cancer cells upon X-ray excitation, *ACS Nano*, 2011, **5**(6), 4679–4687.

76 L. Ma, *et al.*, X-ray excited ZnS: Cu, Co afterglow nanoparticles for photodynamic activation, *Appl. Phys. Lett.*, 2014, **105**(1), 013702.

77 E. Abliz, *et al.*, Novel applications of diagnostic X-rays in activating a clinical photodynamic drug: Photofrin II through X-ray induced visible luminescence from "rare-earth" formulated particles, *J. X-Ray Sci. Technol.*, 2011, **19**(4), 521–530.

78 H. Chen, *et al.*, LiGa5O8:Cr-based theranostic nanoparticles for imaging-guided X-ray induced photodynamic therapy of deep-seated tumors, *Mater. Horiz.*, 2017, **4**(6), 1092–1101.

79 X. Chen, *et al.*, Study of copper-cysteamine based X-ray induced photodynamic therapy and its effects on cancer cell proliferation and migration in a clinical mimic setting, *Bioact. Mater.*, 2022, **7**, 504–514.

80 X. Yu, *et al.*, CT/MRI-Guided Synergistic Radiotherapy and X-ray Inducible Photodynamic Therapy Using Tb-Doped Gd-W-Nanoscintillators, *Angew. Chem.*, 2019, **131**(7), 2039–2044.

 © 2023 The Author(s). Published by the Royal Society of Chemistry